





**UNIVERSITA' DELLA CALABRIA**

Dipartimento di Ingegneria Meccanica, Energetica e Gestionale

**Scuola di Dottorato Pitagora**

**Indirizzo**

Ingegneria Meccanica

*Con il contributo del*

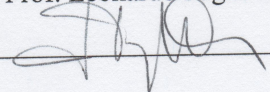
**Ministero dell'Istruzione, dell'Università e della Ricerca (MIUR)**

**CICLO XXVI**

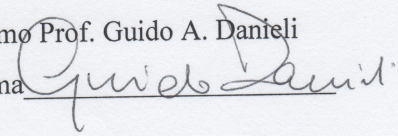
**IMAGE-GUIDED ROBOTIC SYSTEM FOR PRECISION BIOPSY**

**Settore Scientifico Disciplinare Bioingegneria Industriale ING-IND/34**

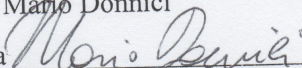
**Coordinatore:** Ch.mo Prof. Leonardo Pagnotta

Firma 

**Supervisore:** Ch.mo Prof. Guido A. Danieli

Firma 

**Dottorando:** Dott. Mario Donnici

Firma 



# Acknowledgement

The author would like to thank the following people for their contribution towards this project:

- Prof. Guido Danieli, my supervisor, for his guidance and help throughout the project, his steady hand, calm nature and wisdom without which I would have not reached this point;
- Prof. Maurizio Muzzupappa my thesis supervisor for his helpfulness and his assistance;
- Prof. Beno Benhabib for the opportunity to work in his lab and for his guidance in facing optimization problems;
- PhD Gianluca Gatti, for his assistance in understanding principles of robotics and his willingness.
- PhD Michele Perrelli and Sebastiano Meduri for their help in developing the electronic components of the system and the software.
- Diego Pulice and Renato Bentreto of the Mechanical Departments Workshop for the manufacturing of the project parts.
- Staff of the Mesere Medical Centre for their assistance and the use of CT scan system.

# Contents

<b>1. Introduction.....</b>	<b>12</b>
1.1 Thesis Overview .....	12
1.2 Motivation .....	13
1.3 Biopsy Procedure .....	13
1.4 Computer Assisted Biopsy Procedure.....	16
1.5 Image-Guided Percutaneous Procedures .....	18
1.6 Rationale .....	26
<b>2. Robotic System Overview.....</b>	<b>27</b>
2.1 Direct Kinematic.....	30
2.2 Joint's Architecture.....	34
2.3 End-Effectors .....	35
2.4 Electronic Control .....	37
2.5 Braking System Design .....	38
2.6 Brake Theoretical Analysis .....	40
2.7 Numerical Simulations and Testing .....	45
2.8 Navi-Robot Calibration .....	47
<b>3. Computer Vision Theory .....</b>	<b>50</b>
3.1 The Camera Projection Matrix.....	51
3.2 2D to 2D Case .....	52
3.3 The Direct Linear Transform Method (DLT).....	52
3.4 3D to 2D Case .....	54
3.5 The Camera Model .....	55
3.6 Basic Pinhole Camera Model .....	56
3.7 Epipolar Geometry.....	58
3.8 Fundamental Matrix.....	60
3.9 Triangulation .....	61
<b>4. Fluoroscopy Based Biopsy .....</b>	<b>61</b>
4.1 C-Arm Fluoroscopy System Overview .....	62
4.2 Stereo Fluoroscopy.....	64
4.3 System Overview and Working Principle .....	66
4.4 Camera Calibration.....	70
4.5 Optical Navigator User Interface and Software .....	73
4.6 End-effector and Needle Orientation Determination .....	74
4.7 Targeting Computation.....	77
4.1 GUI Design and Operation .....	80
<b>5. CT Based Biopsy .....</b>	<b>81</b>
5.1 Graphical User Interface.....	82
5.2 Procedure Workflow for Registration Strategy I .....	83
5.3 Procedure Workflow for Registration strategy II .....	84
5.4 Targeting and Coordinate System Transformation.....	87
<b>6. Testing and Results .....</b>	<b>88</b>

6.1	Laboratory Testing.....	89
6.2	Setup I: Calibration and Targeting.....	89
6.3	Optical Localizer Accuracy.....	90
6.4	Calibration Procedure Accuracy.....	92
6.5	Targeting.....	93
6.6	Setup II: Registration and Targeting.....	94
6.7	Error Propagation.....	97
<b>7.</b>	<b>Conclusions and Recommendations.....</b>	<b>98</b>
7.1	Challenges, Future Improvements and Recommendations.....	98
7.2	Conclusion.....	99
	<b>Bibliography.....</b>	<b>101</b>

## List of Figures

Figure 1:	Fine-needle aspiration.....	14
Figure 2:	Core-needle biopsy.....	14
Figure 3:	Vacuum-assisted biopsy.....	15
Figure 4:	Image-guided biopsy.....	15
Figure 5:	Diagram of an image-guided robot-assisted percutaneous procedure.....	19
Figure 6:	System by Stoianovici et al. [21].....	21
Figure 7:	Needle-guide by Radeka [22].....	22
Figure 8:	Device by Cadeddu et al. [23].....	23
Figure 9:	ROBOPSY™ system [24].....	23
Figure 10:	ultrasound-guided robotic system by Hong et al [30].....	26
Figure 11:	Navi-Robot schematic representation.....	27
Figure 12:	Navi-Robot kinematic model.....	28
Figure 13:	four bar linkages scheme.....	31
Figure 14:	Joint's architecture.....	34
Figure 15:	CAD models of some of the end effectors for orthopedic procedures, being b the pointer, c and d the sawing guide, e the bone clamp, and f and g the drilling guides.....	36

Figure 16: End-effector needle holders.....	36
Figure 17: Needle’s cap for friction adjustment.....	37
Figure 18: brake system unlocked position .....	38
Figure 19: brake system locked position .....	38
Figure 20: Brake system assembly prototype .....	39
Figure 21: Braking current load.....	40
Figure 22: Brake's shoe geometry.....	41
Figure 23: Brake’s shoe pressure load.....	42
Figure 24: Brake’s shoe static equilibrium .....	44
Figure 25: Brake system multi-body cad model .....	45
Figure 26: Housing’s velocity during braking.....	46
Figure 27: Brake system experimental test.....	47
Figure 28: Navi-Robot prototype .....	48
Figure 29: Navi-Robot calibration setup .....	49
Figure 30: Basic pinhole camera model.....	56
Figure 31: Epipolar geometry.....	59
Figure 32: C-arm fluoroscopy system’s elements .....	62
Figure 33: Optical coupling system.....	63
Figure 34: C-arm fluoroscopy system setup.....	64
Figure 35: stereovision fluoroscopy .....	65
Figure 36: C-arm Fluoroscopy system calibration .....	67
Figure 37: Biopsy procedure fluoroscopy based setup .....	70
Figure 38: Calibration ring template.....	72
Figure 39: Optical navigator user interface .....	74
Figure 40: Needle system coordinates.....	75

Figure 41: Needle system coordinate reconstructed .....	76
Figure 42: Needle path planning .....	78
Figure 43: Rotation angles and planes.....	79
Figure 44: C-arm fluoroscopy system user interface.....	81
Figure 45: CT scan user interface .....	82
Figure 46: Biopsy procedure CT based setup .....	84
Figure 47: Biopsy procedure CT based setup using registration strategy II.....	86
Figure 48: Optical marker (left) F-cam calibration setup (right).....	90
Figure 49: known distances between marker.....	91
Figure 50: Needle targeting procedure.....	94
Figure 51: CT scan of the rigid object simulating the patient.....	95
Figure 52: Registration strategy .....	96

## List of Tables

Table 1: Navi-Robot geometric parameters.....	29
Table 2: Navi-Robot D-H parameters.....	29
Table 3: Optical navigator accuracy results.....	91
Table 4: Calibration accuracy result .....	92
Table 5: F-cam accuracy result.....	93
Table 6: F-cam based targeting accuracy result.....	94
Table 7: CT based targeting accuracy result .....	96





# Abstract

The goal of this research is the development of a robotic system for needle biopsy guidance under fluoroscopy and computed tomography (CT). The system aims to minimize patient-surgeon radiation exposure, achieving more accurate biopsy diagnosis, lower patient discomfort, and shorter procedure time. Currently, needle biopsy is performed by free-hand passage of the biopsy needle from the skin surface to the area that must be analyzed. The main problem with free-hand method is the limited accuracy when initially the biopsy needle must be aligned, when the planned needle trajectory must be followed and finally, when the physician releases the needle that can drift or tilt away from the desired path due to gravity, particularly when first starting the insertion. Additionally, direct irradiation to the hand of the physician has been considered to be a disadvantage of this modality, since it can result in high cumulative effective doses of radiations.

The robotic system used in this project to guide the needle is the Navi-Robot, a 6-degree of freedom (DoF) hybrid parallel/serial prototype of robot provided by a novel braking system, which was design and manufactured during this study, to allow the robot working both as measurement device and as robot.

The first topic investigated in this research was performing a fluoroscopy-based biopsy procedure using the Navi-Robot. To this end, a stereovision setup was built and calibrated using a single camera simulating a C-arm fluoroscopy system, an optical localizer and the relative software as well as a graphical user interface. The system, implementing the stereovision theory, allows reconstructing the 3D locations of the needle entry point and the target point selected by the surgeon in the fluoroscope image space. Thus, performing a registration procedure, or rather a coordinates transformations, the 3D coordinates are mapped from the image space to the robot space and the desired needle path as well as the depth of penetration are calculated. Finally, the

position and the orientation of the end-effector carrying the needle-guide is adjusted accordingly, allowing the surgeon inserting the needle until the calculated depth is reached. The second topic investigated was performing a CT based biopsy procedure using the Navi-Robot. To achieve this goal was necessary to register the coordinates of the needle entry point and of the target from the CT space to the robot space. Using rigid marker placed on a phantom simulating the patient two different strategies for registration were tested: the first one was performed using the Navi-Robot as measurement system and its end-effector as a touch probe to localize the markers; the second strategy was implemented providing the end-effector by optical markers and using an optical localizer to track both the marker on the phantom and the marker on the end-effector. Once the registration was performed, the desired needle path was computed to adjust the needle-guide of the robot allowing the surgeon inserting the needle. Simulating the C-arm fluoroscopy system with a digital camera, needle placement accuracies of 10 mm was achieved within the calibrated volume. Using CT images and the optical localizer for the registration procedure, needle placement accuracies of 4 mm was achieved, while using the robot for the registration procedure an accuracy of 2 mm was obtained in the simulated environment.

# 1. Introduction

## 1.1 Thesis Overview

Chapter 1 presents background on biopsy techniques. Relevant needle-positioning systems developed during the last decade are discussed. Chapter 2 describes the Navi-Robot, the prototype robotic system used to position the needle-guide, as well as its main components and working principle. Moreover, it discusses a novel braking system designed and tested for the robot prototype. Chapter 3 describes the theory implemented to mathematically describe cameras and use them for relative positioning. This leads to Chapter 4 where the elements of the system used to perform a needle biopsy using the robotic system under C-arm fluoroscopy guidance are described. It also depicts the calibration techniques used to implement the stereovision using a single camera and the reasons for their use in the project. This chapter also covers the mathematical computations implemented to rotate and translate the needle-guide for accurate targeting and description of the graphical interface developed for the procedure. In Chapter 5, the procedure used to guide a needle biopsy with the Navi-Robot under CT is shown as well as the software to localize the markers used for the registration procedure, or rather to map the coordinates of the target point from the CT-space to the robot space. Chapter 6 describes the experiments setup and reports on the results obtained. The final chapter presents the conclusions and recommendations of the project. The shortcomings of the designed system are also commented on.

## **1.2 Motivation**

Increased use of intraoperative fluoroscopy exposes the surgeon to significant amounts of radiation. The average yearly exposure of the public to ionizing radiation is 360 millirems (mrem), of which 300 mrem is from background radiation and 60 mrem from diagnostic radiographs. A chest radiograph exposes the patient to approximately 25 mrem and a hip radiograph to 500 mrem. A regular C-arm exposes the patient to approximately 1,200 to 4,000 mrem/min. The surgeon may receive exposure to the hands from the primary beam and to the rest of the body from scatter. Recommended yearly limits of radiation are 5,000 mrem to the torso and 50,000 mrem to the hands. Exposure to the hands may be higher than previously estimated, even from the mini C-arm [1].

Needle biopsy is one of the intraoperative procedures that mainly cause a large amount of ionizing radiation absorption when is performed using the free-hand method. Performing a biopsy in fact requires the physician first to adjust the biopsy needle by hand, then to partially insert it towards the target, finally to proceed with further insertion of the needle, checking its position by scanning the area as necessary.

Potential decreases in radiation exposure and increase in accuracy can be accomplished by using instruments such as robot or positioning systems.

These tools have the potential to improve the precision and capabilities of the physicians during surgical procedures. Therefore, a robotic system able to work with as many as possible diagnostic imaging equipment such as: CT-scan, ultrasound, fluoroscopy, MRI, etc., would have a great impact on the surgery scenario.

## **1.3 Biopsy Procedure**

During a needle biopsy, the surgeon uses a special needle to extract cells from a suspicious area. A needle biopsy is often used on tumors that the doctor can

feel through your skin, such as suspicious breast lumps and enlarged lymph nodes. When combined with an imaging procedure, such as X-ray, needle biopsy can be used to collect cells from a suspicious area that can't be felt through the skin. Needle biopsy procedures include:

- **Fine-needle aspiration.** During fine-needle aspiration, a long, thin needle is inserted into the suspicious area. A syringe is used to draw out fluid and cells for analysis.

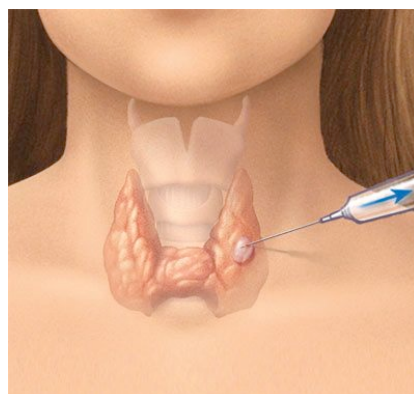


**Figure 1: Fine-needle aspiration**

- **Core needle biopsy.** A larger needle with a cutting tip is used during core needle biopsy to draw a column of tissue out of a suspicious area.

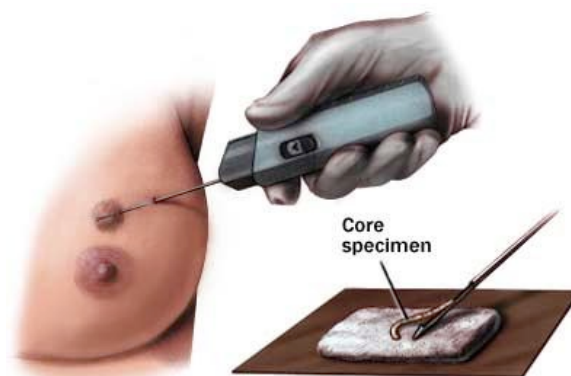


**Figure 2: Core-needle biopsy**

- **Vacuum-assisted biopsy.** During vacuum-assisted biopsy, a suction device increases the amount of fluid and cells that is extracted through the needle. This can reduce the number of times the needle must be inserted to collect an adequate sample.

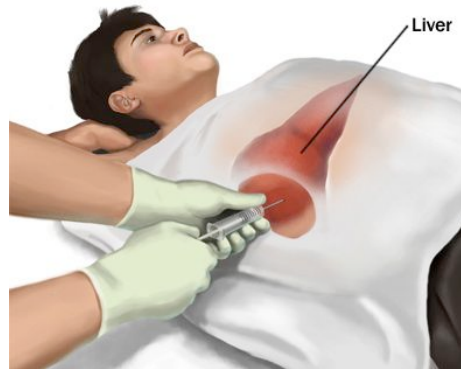


**Figure 3: Vacuum-assisted biopsy**

- **Image-guided biopsy.** Image-guided biopsy combines an imaging procedure, such as X-ray, computerized tomography (CT), magnetic resonance imaging (MRI) or ultrasound, with a needle biopsy. Image-guided biopsy allows your doctor to access suspicious areas that can't be felt through the skin, such as abnormalities on the liver, lung or prostate. Using real-time images, the doctor can make sure the needle reaches the correct spot.

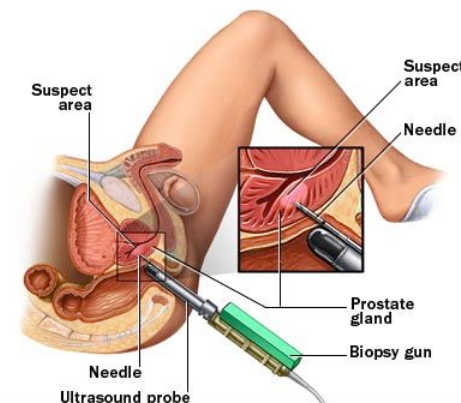


**Figure 4: Image-guided biopsy**

One of the more difficult initial decisions is selecting the biopsy site. Generally, lesions with the most advanced inflammatory changes should be chosen; evolutionary changes may take several days and a too-early biopsy may reveal only nonspecific features. For blistering diseases, the reverse is true; the earlier the lesion, the more specific the histopathology. Consequently, only the newest vesicles and blisters should be biopsied, usually within 48 hours of their appearance. Older lesions with secondary changes such as crusts, fissures, erosions, excoriations, and ulcerations should be avoided since the primary pathological process may be obscured. For non-bullous lesions, the biopsy should include maximal lesion skin and minimal normal skin [2].

## **1.4 Computer Assisted Biopsy Procedure**

A number of modern clinical practices involve percutaneous (“through the skin”) diagnosis and local therapies, where a tubular device (needles, catheters, tissue ablation probes, etc.) has to be inserted deep into soft tissue to reach a target. There are several applications for percutaneous needle insertion such as biopsies [3], regional anesthesia, blood sampling [4], neurosurgery [5] and brachytherapy [6]. The effectiveness of a treatment and the success or precision of a diagnosis is highly dependent on the accuracy of percutaneous insertion [7]. There is not a defined tolerance for the accuracy of needle insertion in clinical practice and in general, insertions with less needle misplacement result in more effective treatment [8] or increase the precision of diagnosis. The desired performance depends on the application. In procedures such as biopsy (for prostate, kidney, breast and liver), brachytherapy and anesthetic, placement accuracy of millimeters is desirable while in brain, fetus, eye and ear procedures placement accuracy of micro-millimeter is preferable. Clinical studies have revealed that targeting error (needle misplacement) may be due to imaging limitations, image misalignments, target uncertainty, human errors, target movement due to tissue deformation and needle deflection [9]. In Ref.



[9], for imaging misalignment of  $\pm 5$  mm in only one view, a targeting error of about 10 mm was calculated. Furthermore, in a percutaneous procedure, the target might be in the millimeter neighborhood of another organ, vessel or nerve. Therefore, extra caution is required to avoid any damage or spread of a disease, which in turn may lead to subsequent complications (e.g., seed migration) that may even be fatal [10]. Some of the desired accuracies may be achieved using current tools and models but accurate needle placement for many other applications requires much more research and development. Real-time visualization and high precision imaging techniques can increase the performance of the surgeon in navigating the tool and tracking the target [11]. Advanced mechanical tools that consider the constraints imposed by anatomy using haptic feedback and those that reduce or remove human errors due to fatigue, hand tremor and problems in hand/eye coordination can contribute to reduction in targeting error [12]. Medical simulators that can accurately model a clinical procedure are of great advantage for training medical residents, predicting the out-come of complex procedures and practicing new procedures. Percutaneous therapies are constrained procedures where target visibility, target access and tool maneuverability in addition to physiological changes to the target are key issues. During some conventional needle insertion procedures, the surgeon relies on kinesthetic feedback from the tool (needle or catheter) and his or her mental 3D visualization of the anatomical structure [13]. Real-time imaging techniques that are used in some procedures can improve target visibility. However, human errors [10], imaging limitations, target uncertainty [9], tissue deformation and needle deflection [14] are a few known problems that contribute to needle misplacement in percutaneous procedures. Human errors may be related to poor techniques and insufficient skills of a physician. Target uncertainty may be caused by patient motion, physiological or geometry related problems [9]. Despite the availability of different imaging modalities to improve visualization; there are several factors such as high cost, poor resolution, probe availability, X-ray exposure, material compatibility, reliable

real-time image processing techniques, etc. that may limit application of imaging in some clinical and research studies. A few examples of these limitations are working with robots where MRI is the imaging modality (magnetic interference), using artificial phantoms when the imaging modality is ultrasound (acoustic properties), and using camera when performing *ex vivo* experiments (non-visibility of target). Needle deflection is generally due to the bevel tip and diameter of the needle [15]. The tissue, into which the needle is inserted, may also contribute to needle deflection. The factors that affect tissue deformation include mechanical properties of soft tissue, the contact force of the needle tip, and frictional forces between the tissue and the needle shaft [16]. Other causes of inaccuracy in percutaneous therapies are physiological changes in the organ between the planning and treatment phases, glandular swelling during the operation. In addition, difference in tissue types involved in each procedure, differences in mechanical properties of healthy and diseased tissue, changes of mechanical properties when tissue is damaged and variability of soft tissue properties for the same organ in different patients.

## **1.5 Image-Guided Percutaneous Procedures**

To date, a number of researchers have explored ways to improve the process of needle insertion in soft tissue using robotics and medical imaging in order to improve the accuracy of the procedure.

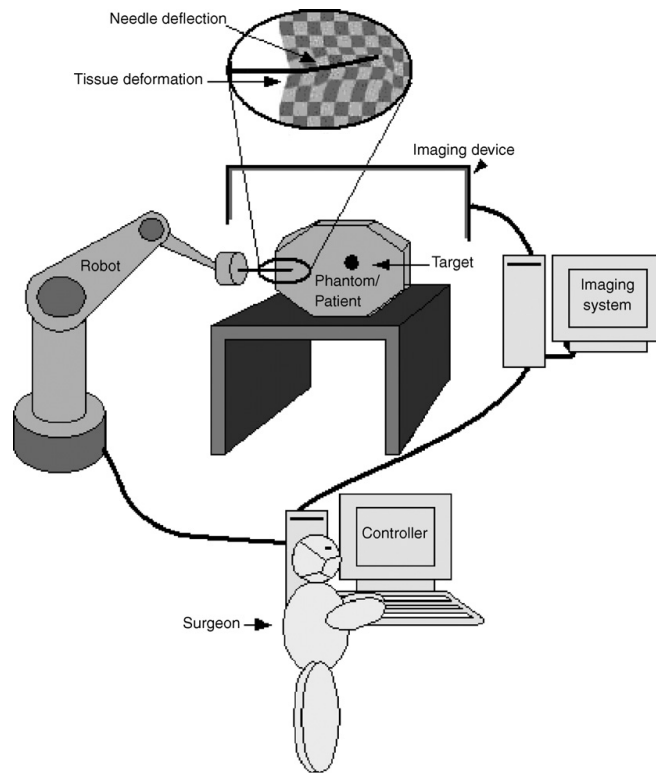


**Figure 5: Diagram of an image-guided robot-assisted percutaneous procedure**

Fig. 5 shows a schematic diagram of an image-guided robot-assisted percutaneous procedure. Some of these techniques, such as CT and MRI, are overly expensive and can only be implemented in highly equipped facilities. Techniques also exist that are used for keeping the object at the correct position and alignment during insertion. Rigid aligning and laser-guided methods are the most common.

Initial applications of robots in urologic surgery have demonstrated their potential in aiding surgeons. The chief advantages of robotic manipulation of surgical tools are accurate registration of medical images, consistent movement free of fatigue or tremor, the ability to work in environments unfriendly to surgeons, and the ability to position instruments quickly and accurately.

Surgical robots can be divided into two categories: surgeon driven systems and image-guided systems. Surgeon driven systems rely directly on the surgeon's movement and simulate that movement by robotic means. Image-guided

systems use a target specified by the surgeon to manipulate instruments in such a way as to reach the specified target. As the system developed in this project fall in the latter category, the focus will be on current image-guided systems applied in surgery.

In 2003, Stoianovici et al. [17] described the development of a robot for radiological percutaneous interventions using computed tomography (CT) for needle biopsy, radio frequency ablation, cryotherapy, and other needle procedures. The system called “AcuBot” is a compact six-degree-of-freedom robot for manipulating a needle or other slender surgical instrument in the confined space of the imager without inducing image artifacts.

In 1994, Potamianos et al. [18] investigated a robotic system to assist the urologist in obtaining intraoperative percutaneous renal access. The system utilized a passive manipulator mounted on the operating table, guided by a C-arm fluoroscopic unit. Registration between the manipulator and C-arm coordinate systems was completed by a personal computer that also displayed the access needle’s trajectory on each fluoroscopic image. The surgeon could then manipulate the robotic arm until the needle’s anticipated trajectory aligned with the target calyx. Experiments evaluated system performance with a targeting accuracy of less than 1.5 mm. The system developed by Bzostek et al. [19] differed mainly from Potamianos’ design in that it used an active robot to manipulate the needle and used bi-planar instead of C-arm fluoroscopy. This system achieved in-vitro accuracy results of 1 mm. Ex-vivo tests on porcine kidneys resulted in an 83% insertion success rate. In-vivo tests on cadaveric porcine and live percutaneous renal access resulted in a 50% success rate with needle deflection, bowing, and rib interference stated as the main problems. This system consisted of a three degree of freedom robot with a needle injector end-effector. Calibration and distortion correction was done after which robot to image-space registration was completed.

Rovetta developed another image-guided robotic system that has been evaluated clinically [20]. This system used external video cameras and TRUS

(trans-rectal ultrasonography) for robot registration. Stoianovici et al. developed a manual system that mimicked and improved on the standard technique used by the urologist during a percutaneous procedure. Similar to the manual surgical technique as keyhole surgery, the skin insertion site, target calyx and needle was superimposed as a single point in a C-arm fluoroscopic image. The needle was held by a novel mechanism driven by a joystick controlled variable speed DC motor enabling automatic needle insertion. The device was locked so the C-arm could be rotated freely to the lateral view. The advantages of this system were that it did not require computer-based vision or a fully actuated robotic system. Accuracies obtained were claimed to be better than that of the standard procedure [21].

Another needle guidance application was that of Radeka, who used CT-guidance and a needle alignment device to position the access needle inside a specified calyx. Bio modeling for pre-surgery planning was performed prior to the access procedure. In fifteen of the seventeen patients, needle placement was performed successfully with the first attempt [22]. The needle alignment device and its exploded view are shown in Fig 6.

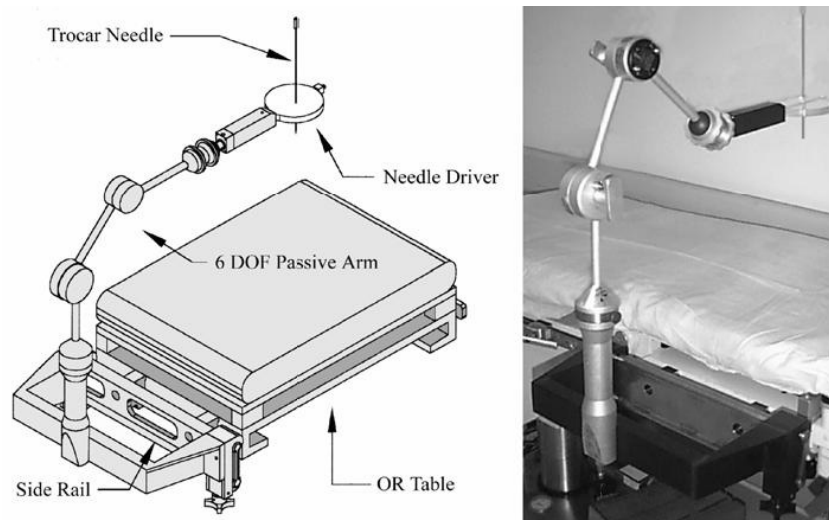


**Figure 6: System by Stoianovici et al. [21]**

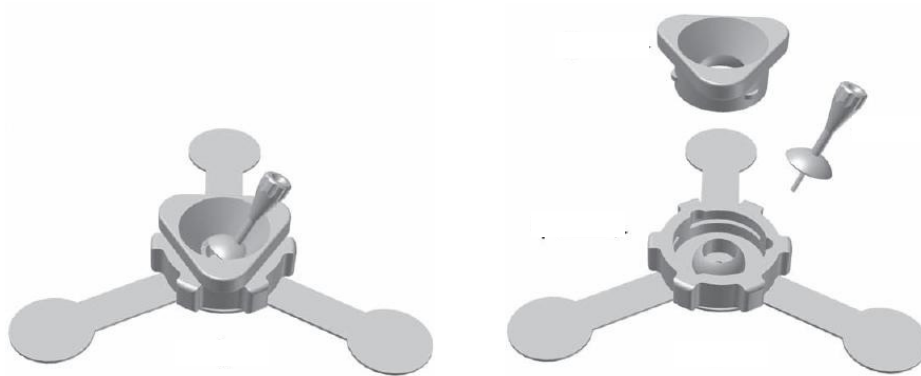


**Figure 7: Needle-guide by Radeka [22]**

Cadeddu and associates improved on Stoianovici's original design. A mechanical system for percutaneous access called PAKY (Percutaneous Access to the Kidney), which is a mechanical stereotactic frame and actuated needle system that can be used as a platform for needle placement, was developed. Superimposed fluoroscopic images of the target, access point and needle were used to align the needle by adjusting the orientation of the C-arm imaging system. Clinical percutaneous access was attained in each of the nine evaluated cases [23]. This system is shown in Fig 8.

Another study is that of the Robopsy™ system, a tele-operated, patient-mounted, disposable needle guidance and insertion system. This system's function is the assistance of radiologists in performing minimally invasive percutaneous biopsies under CT guidance.

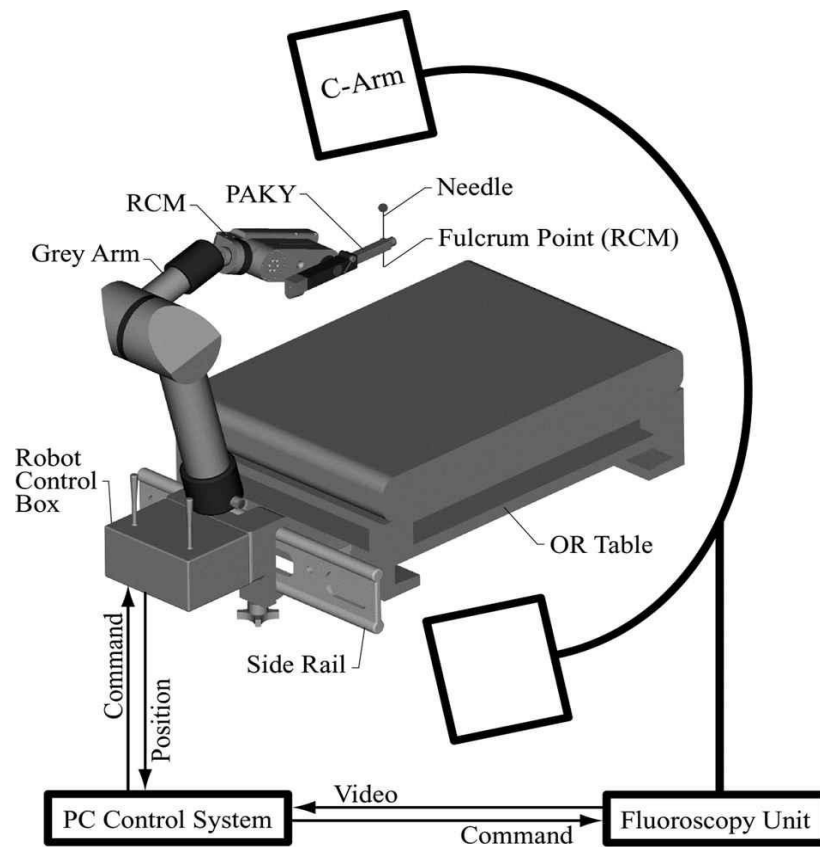


Figure 8: Device by Cadettu et al. [23]

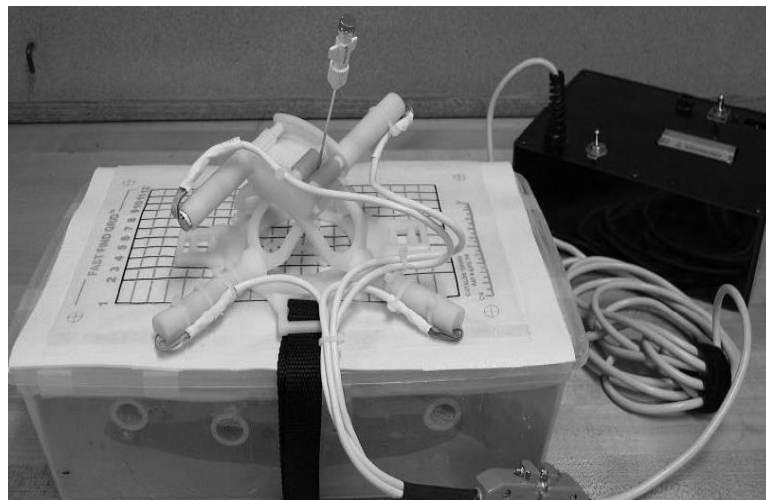


Figure 9: ROBOPSY™ system [24]

This system enables radiologists to automatically adjust needle alignment and

insert the needle without removing the patient from the CT scanner. No automatic needle positioning calculations are done. The surgeon under continuous CT guidance to confirm when correct angular alteration has been completed adjusts the needle remotely [24]. Vaird et al. developed a MRI needle guidance technique where the target point inside the body and the access point on the skin are defined on MRI images, thus defining the required needle trajectory. 3D imaging is used for target visualization, insertion planning and validation of the roadmap. Monochromic CCD (charge-coupled device) cameras sensitive to infrared radiation are used in a stereovision setup to determine needle orientation. Current needle orientation relative to the planned needle orientation is then monitored in near real-time during insertion, thus aiding the surgeon in accurate needle placement. Obtained accuracy was 3 mm [25].

Navab et al. presented an approach for fluoroscopy image-based guidance of a surgical tool towards multiple targets from fixed or variable entry points. The method is based on visual servoing and required no prior calibration or registration. At least 12 images are required for each targeting sequence [26]. A US Patent by Geiger and Navab describes a method by which a biopsy needle is aligned with a target using needle markers from two fluoroscopic images taken in orthogonal C-arm positions. Needle alignment angles are calculated by a computer system in a two-step procedure, where the first alignment angle is computed and set with the C-arm in position 1, and the second alignment angle is and track any other feature such as a medical instrument in the workspace with the cameras fixed in their positions relative to the workspace [27].

An additional US Patent by Regn describes CT apparatus equipped with a laser device marking a guide path on a patient for a medical instrument to be used in a medical procedure such as needle puncturing. The CT apparatus produces a planning image and a guide path is identified within the planning image. A computer, using the planning image, and the path identified, automatically adjusts the position of a light source. If necessary a table, on which a patient is



supported, is positioned so that a beam from the light source is positioned to coincide with the guide path identified on the image. During insertion, the needle is kept in this line of light by the surgeon, thus targeting the defined position [28]. The main problems incurred by most of the mentioned techniques are needle deflection due to tissue resistance and target movement. Techniques that consider these factors are currently being researched. It was not within the scope of this project to take these factors into account, but to verify whether accurate and operationally viable targeting results could be obtained by implementing stereovision theory on fluoroscopic images computed and set with the C-arm in position and also to validate a system able to operate even with CT or other medical imaging systems.

Another US Patent by Peter and associates describes a system for defining the location of a medical instrument relative to features of a medical workspace including a patient's body region. Pairs of two-dimensional images, obtained by two video cameras making images of the workspace along different sightlines, which intersect, are used. After the calibration image pair is made, the fiducial structure is removed. A standard projection algorithm is used to reconstruct the 3D framework of the fiducial structure from the calibration image pair. Appropriate image pairs can then be used to locate and track any other feature such as a medical instrument, in the workspace, so long as the cameras remain fixed in their positions relative to the workspace. The computations are desirably performed with a computer workstation including computer graphics capability, image-processing capability, and providing a real-time display of the workspace as imaged by the video cameras [29].

Hong et al developed a real-time ultrasound-guided needle-insertion medical robot for percutaneous cholecystectomy. The instrument uses intraoperative images and modifies the needle path in real time by using a novel ultrasonic image segmentation technique [30].

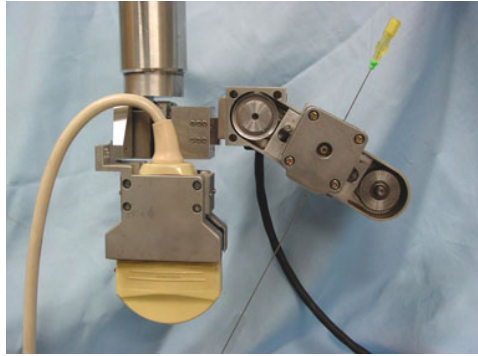


**Figure 10: ultrasound-guided robotic system by Hong et al [30]**

## **1.6 Rationale**

Despite the number of apparent solutions described, only few of the techniques described are currently used in practice, mainly due to their high cost. Each of them, in fact, has been designed to work with a specific medical imaging apparatus or surgical tools. The robotic system proposed, originally designed to perform orthopedic and laparoscopic surgical procedures, is able to guide the needle or other surgical tool, to the correct insertion depth with minimal radiation exposure to the patient and surgery team using standard fluoroscopy, CT or ultrasound. It is important to note that the system does not replace the surgeon, who still plays the main role, choosing the target that must be analyzed, planning the trajectory and inserting the needle once the final position has been reached, granting the surgeon a large range of options.

Moreover both the software and hardware can be easily upgraded, for example adding an additional DoF for needle insertion, and thus implementing a full automatic biopsy procedure. Since the cost was identified as the common restriction for implementation of most new systems, particular attention was paid in order to develop a system able to aid the surgeon to perform a very wide range of medical treatments.

## 2. Robotic System Overview

This chapter gives an overview of the robotic system prototype used, as well as its main specifications and requirements.

The robotic system used to perform needle biopsy, is the Navi-Robot developed by the Department of Mechanical Engineering at University of Calabria in cooperation with one of its spin off: Calabrian High Tech s.r.l. [31]. Originally designed for orthopedic applications, the Navi-Robot is a 6-DOF self-balancing arm. The kinematic structure is hybrid parallel/serial with rotational transducers to measure the relative angle between consecutive linkages. A schematic representation of the actual system is shown in Fig. 11.

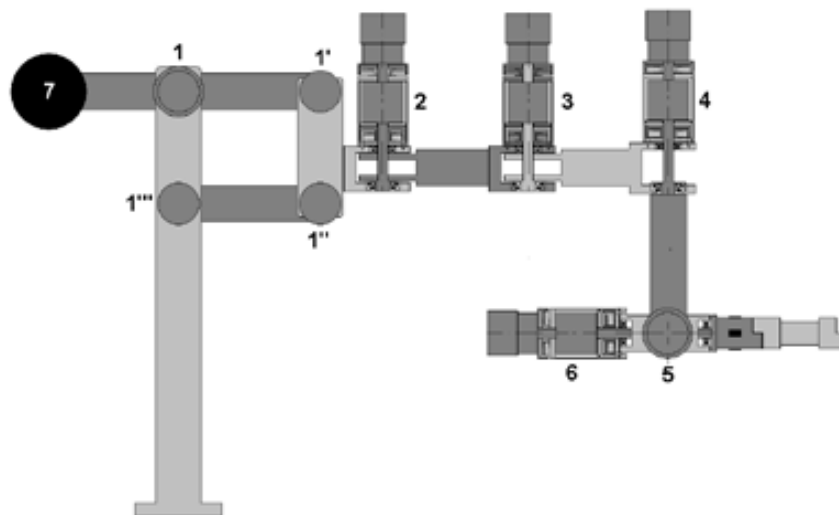


**Figure 11: Navi-Robot schematic representation**

Each joint bears a clutch, a brake, an absolute encoder, and a motor-reducer group. Its kinematic chain is composed of a planar four-bar-linkage with horizontal axes, which provides a single vertical degree of freedom, while a 3-DOF structure mounting parallel vertical axes is linked to the rod of the four-bar-linkage mechanism. To the fourth rotational DOF a fifth hinge with axis perpendicular to the fourth is linked, being the sixth again perpendicular to the

previous, while the axes of the last three hinges meet in a single point, which behaves as a spherical hinge. A schematic view of the 6-DOF arm's structure, with the identification of the base frame  $\{B\}$  and the end effector frame  $\{E\}$  is shown in Fig. 12 in its zero-reference configuration. A kinematic model is formulated, which relates the joints' angles to the end-effector pose in the base frame. The scheme below shows the "zero configuration" for the robot where each encoder is set to 0 while in the following table nominal parameters of the robot are reported.

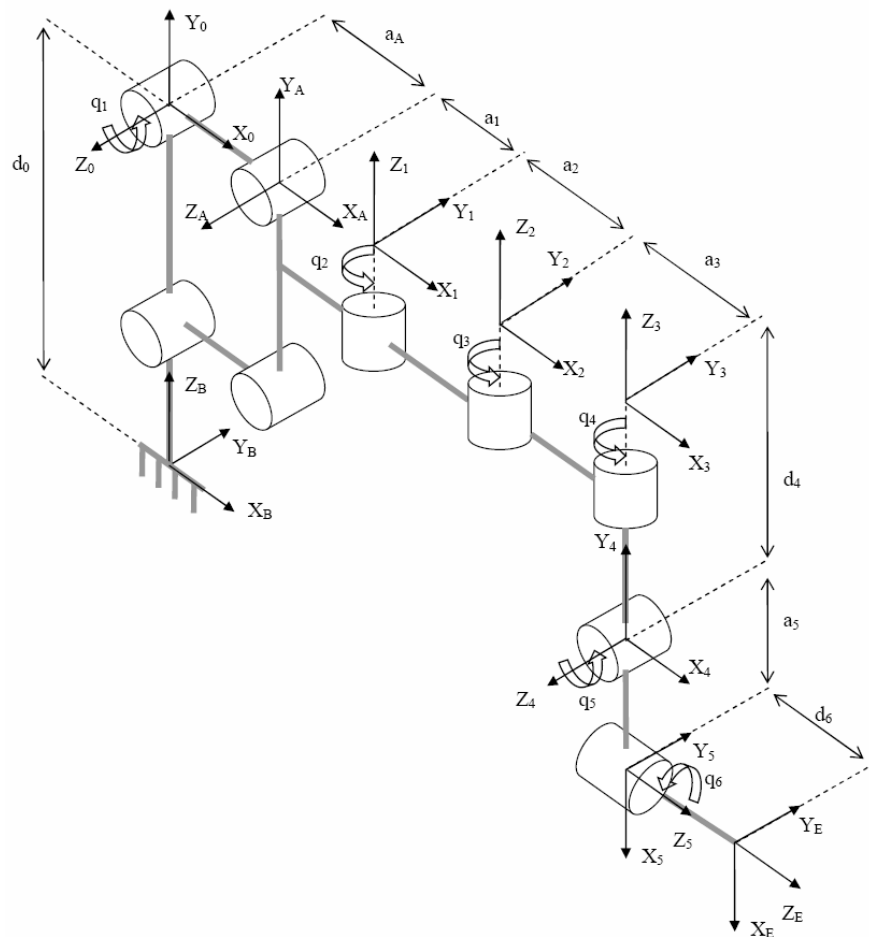


**Figure 12: Navi-Robot kinematic model**

**Table 1: Navi-Robot geometric parameters**

Geometry	Value	Unit	Geometry	Value	Unit
$d_0$	670	mm	$a_2$	470	mm
$a_0$	60	mm	$a_3$	470	mm
$L_1$	400	mm	$d_4$	250	mm
$L_2$	300	mm	$a_6$	70	mm
$L_3$	400	mm	$b_6$	0	mm
$L_4$	300	mm	$c_6$	60	mm
$a_1$	300	mm	$\delta$	$3\pi/2$	rad

For the serial part of the robot the following D-H parameters were estimated:

**Table 2: Navi-Robot D-H parameters**

Transformation	$\theta_i$	$d_i$	$\alpha_i$	$a_i$
2	$q_2$	0	$a_2$	0
3	$q_3$	0	$a_3$	0
4	$q_4$	$d_4$	0	$\pi/2$
5	$q_5$	0	0	$\pi/2$
e	$q_6$	$d_e$	0	0

The workspace of each arm has been evaluated to be an approximate box of sizes  $400 \times 400 \times 400 \text{ mm}^3$ . Kinematic performance of the system in terms of the theoretical resolution is evaluated when 16 bit encoders are used as revolute joint sensors. Resolution, which is defined according to the already quoted International Standard ISO 9283, as the smallest incremental movement of

which the robot end effector is capable of sensing, is a theoretical characteristic and may be evaluated given the configuration and the nominal dimensions of the linkage. It is affected by the individual encoders' resolution and depends on the instantaneous arm configuration. An approximate relation provides an estimate of the arm's resolution as follows:

$$\mathbf{RS} \approx \sum_{i=1}^N \mathbf{d}_i(\mathbf{q}) \cdot \delta \mathbf{q}_i \quad [1]$$

where  $d_i$  is the distance between the end effector endpoint and the revolute axis of the  $i^{\text{th}}$  joint and it depends on the arm configuration, i.e. on the vector of joints' angles  $\mathbf{q} = [q_1, q_2, q_3, q_4, q_5, q_6]^T$  while  $\delta q_i$  is the  $i^{\text{th}}$  transducer resolution. Since the endpoint displacement, resulting from the smallest incremental motion of the joints, varies significantly throughout the workspace, equation 1 is practically used for some particular system's configuration where may be easily evaluated, e.g. in the zero-reference configuration. In such a reference configuration, as shown in Fig. 12 equation 1 gives an estimate of the theoretical maximum resolution for the end effector endpoint. Hence, when adopting 16 bit encoders' with a resolution of about 0.0055 degrees per step, equation 1 gives a maximum value for the resolution of 0,3 mm.

## 2.1 Direct Kinematic

As for the kinematic model, the transformation between frame {B} on the four-bar-linkage end frame {1} we can consider the following scheme

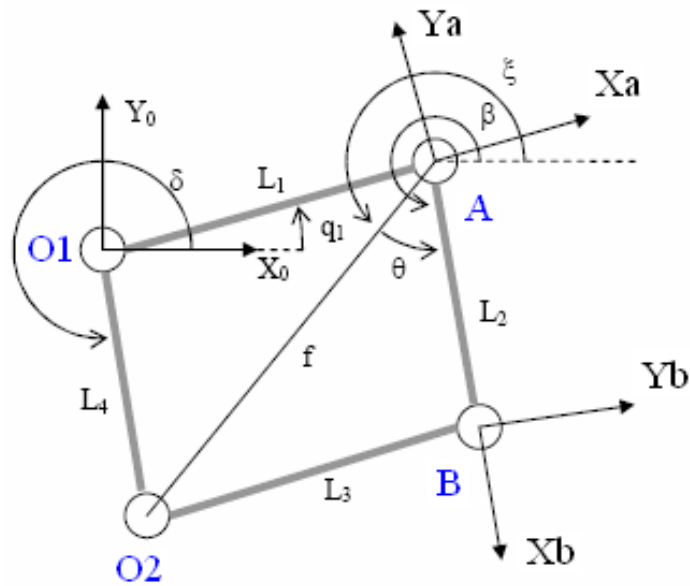


Figure 13: four bar linkages scheme

Due to geometric and assembly errors, the lengths of the bars:  $L_1$ ,  $L_2$ ,  $L_3$ ,  $L_4$ , could not be exactly equal to the nominal values, as well as the fixed hinges  $O_1$ ,  $O_2$  could not be exactly located at the nominal positions. These errors can lead to a rotation, not desired in the original design, of the bar  $L_2$  with respect the horizontal (dotted line in Fig. 13) and represented by the angle  $\beta$ . This angle depends on: the lengths of the bars, the angle  $\delta$ , and on the joint's angle  $q_1$ . The relationship between the angle  $\beta$  and  $q_1$  can be calculated applying the sum of vectors on the triangle  $O_1$ , A,  $O_2$ . For the four bar linkages, in the table below the nominal parameters with the error parameters associated are reported.

Nominal Parameter	Error Parameter Associated
$q_1$	$\delta k_5$
$L_1$	$\delta k_6$

L2	$\delta k_7$
L3	$\delta k_8$
L4	$\delta k_9$
$\delta$	$\delta k_{10}$

Hence calling  $f$  the vector between the hinges  $O_2$  and A, we can state the following relations:

$$f = \sqrt{\begin{aligned} & ((L_4 + \delta k_9) \sin(\delta + \delta k_{10}) - (L_1 + \delta k_6) \sin(q_1 + \delta k_5))^2 + \dots \\ & \dots ((L_4 + \delta k_9) \cos(\delta + \delta k_{10}) - (L_1 + \delta k_6) \cos(q_1 + \delta k_5))^2 \end{aligned}} \quad [2]$$

$$\xi = \arctan \frac{((L_4 + \delta k_9) \sin(\delta + \delta k_{10}) - (L_1 + \delta k_6) \sin(q_1 + \delta k_5))^2}{((L_4 + \delta k_9) \cos(\delta + \delta k_{10}) - (L_1 + \delta k_6) \cos(q_1 + \delta k_5))^2} \quad [3]$$

$$\theta = \pm \arccos \frac{-(L_3 + \delta k_8)^2 + f^2 + (L_2 + \delta k_7)^2}{2f(L_2 + \delta k_7)} \quad [4]$$

$$\beta = \xi + \theta \quad [5]$$

We can now state the equations which describe the direct kinematic of the robot or rather which can allow to define the pose (translation and rotation) of the end-effector with respect the base robot coordinate system.

$$T_{B0} = R_Z(\delta k_1) * D_Z(d_0 + \delta k_2) * D_X(a_0 + \delta k_3) * R_X(\pi/2 + \delta k_4) \quad \text{DH} \quad [6]$$



$$T_{0A} = R_z(q_1 + \delta k_5) * D_x(L_1 + \delta k_6) \quad \text{DH plane} \quad [7]$$

$$T_{AB} = R_z(\beta - q_1 - \delta k_5) * D_x(L_2 + \delta k_7) \quad \text{DH plane} \quad [8]$$

$$T_{B1} = R_z(\pi/2 + \delta k_{11}) * D_z(\delta k_{12}) * D_x(a_1 + \delta k_{13}) * R_x(-\pi/2 + \delta k_{14}) \quad \text{DH} \quad [9]$$

$$T_{12} = R_z(q_2 + \delta k_{15}) * D_x(a_2 + \delta k_{16}) * R_x(\delta k_{17}) * R_y(\delta k_{18}) \quad \text{DH mod} \quad [10]$$

$$T_{23} = R_z(q_3 + \delta k_{19}) * D_x(a_3 + \delta k_{20}) * R_x(\delta k_{21}) * R_y(\delta k_{22}) \quad \text{DH mod} \quad [11]$$

$$T_{34} = R_z(q_4 + \delta k_{23}) * D_z(-d_4 + \delta k_{24}) * D_x(\delta k_{25}) * R_x(\pi/2 + \delta k_{26}) \quad \text{DH} \quad [12]$$

$$T_{45} = R_z(q_5 - \pi/2 + \delta k_{27}) * D_z(\delta k_{28}) * D_x(\delta k_{29}) * R_x(-\pi/2 + \delta k_{30}) \quad \text{DH} \quad [13]$$

$$T_{5t} = R_z(q_6) * D_z(c_6 + \delta k_{31}) * D_y(b_6 + \delta k_{32}) * R_y(5/4 * \pi + \delta k_{33}) * D_z(-a_6 + \delta k_{34}) * R_x(\delta k_{35}) * R_z(\delta k_{36}) \quad [14]$$

where:

$R_i$  elementary rotation about the axis  $i$

$D_i$  translation along the axis  $i$

$\delta K_i$  error for  $i$ -parameter

For the transformations:  $T_{B0}$ ,  $T_{0A}$ ,  $T_{AB}$ ,  $T_{B1}$ ,  $T_{34}$ ,  $T_{45}$ ,  $T_{5t}$  the Denavit-Harteberg notation was used where:

$$T_{i-1,i} = R_z(\theta_i) * D_z(d_i) * D_x(a_i) * R_x(\alpha_i) \quad [15]$$

As for the transformation  $T_{12}$ ,  $T_{23}$  the modified Denavit-Harteberg notation was used, where:

$$T_{i-1,i} = R_z(\theta) * D_x(r) * R_x(\alpha) * R_y(\beta) \quad [16]$$

The global transformation matrix can be expressed by:

$$T_{Bt} = T_{w0} * T_{0A} * T_{AB} * T_{B1} * T_{12} * T_{23} * T_{34} * T_{45} * T_{5t} \quad [17]$$

## 2.2 Joint's Architecture

As mentioned before and as it can be seen in the figure below (Fig. 14), each joint of the robot comprises, starting from the top to the bottom, the following components: a motor-reducer, a step motor, a first braking system, an absolute encoder, and a second braking system identical to the previous one. The joint's frame is connected to a shaft, supported by two bearings, whose axis is orthogonal to link's axis on which all the components are connected to. The braking system placed above works as a clutch and allows coupling or decoupling the step motor to the joint's axes. The second braking system instead, is directly connected to the shaft and works as simple brake.

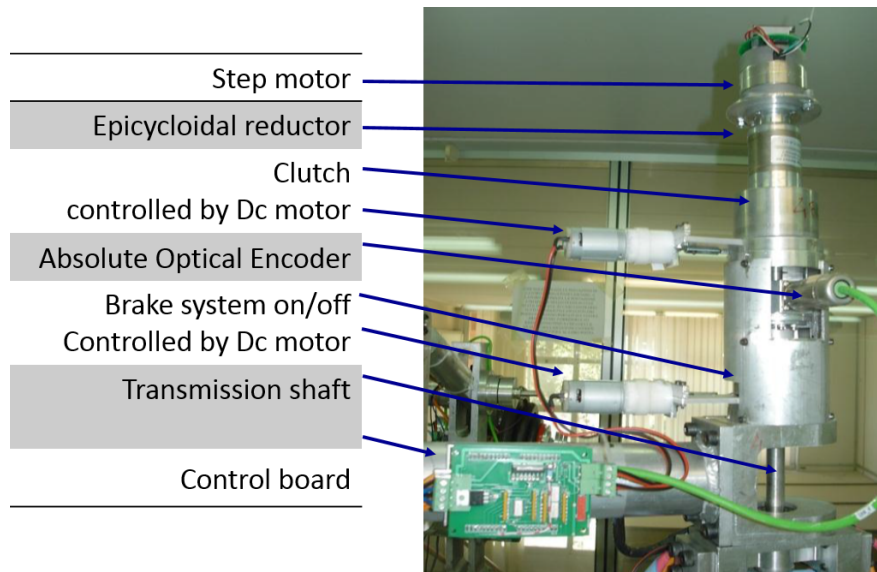


**Figure 14: Joint's architecture**

The braking system plays an important role in the Navi-Robot architecture, since accordingly to the idea of the designers this robot must be able to turn itself into a measurement system and vice versa. This particular feature makes

the Navi-Robot different from other surgical robot or image-guided robotic devices allowing a wide range of operations and at the same time provides surgeons great flexibility and freedom of choice. The aim of the designers in fact is not replacing the surgeon, but to assist him in placing/guiding instruments and planning interventions. In order to achieve this goal the braking system should work mainly as a mechanical switch in static conditions, since it must keep the joints in a desired position. The brake also should provide high brake torque, low energy consumption and low amount of space. At the state of the art none of the commercial devices meet these requirements, thus a new concept brake was designed.

## **2.3 End-Effectors**

Since the Navi-Robot was designed to perform several different surgery procedures, such as: laparoscopic, orthopedic, oncologic etc., several different end-effectors can be used (Fig 15) often, more than one is required for the same medical procedure. Thus, a system allowing exchanging the tool, without recalibrating and re-programming every time the robot could be very helpful. That being so, a first hardware solution, which was designed during this project but not manufactured yet, is providing the system with an intermediate stage (frame a2), which can be sterilized as well, so that the end-effector can be replaced during a surgery without risk of contamination. Thus, both the intermediate end-effector and all the various end-effectors must be purely mechanical components, while the unsterile part of the end effector (a1), which belong to the last link of the robot, must be able to recognize which end-effector is installed.

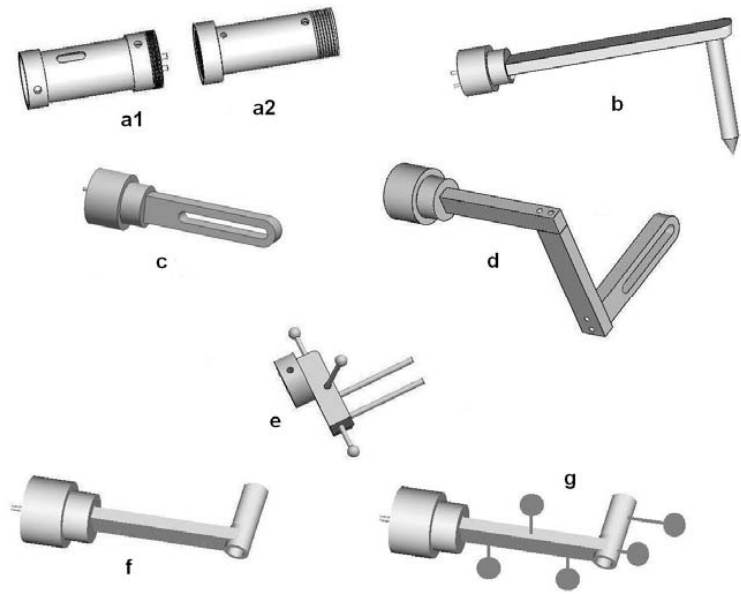


**Figure 15: CAD models of some of the end effectors for orthopedic procedures, being b the pointer, c and d the sawing guide, e the bone clamp, and f and g the drilling guides**

In this project, the end-effector used to hold the needle during the positioning and insertion procedure, (type g in Fig. 15) was simply locked into the shaft of link 6° as well as has been done for the end-effector used for the calibration procedure that will be discussed in section 2.8.

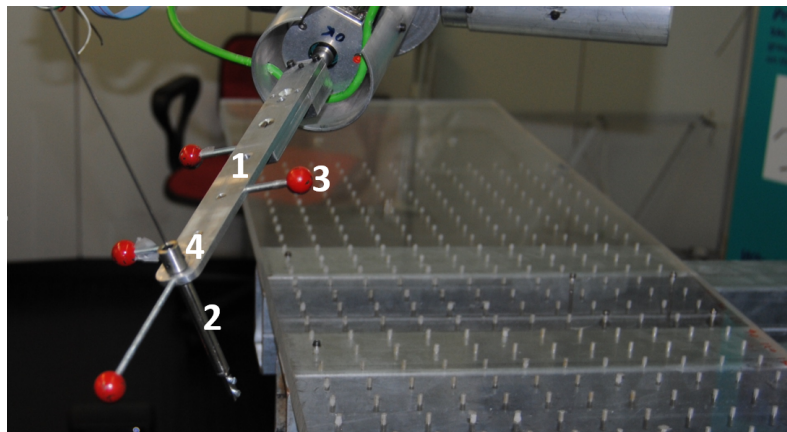


**Figure 16: End-effector needle holders**

As can be seen in Fig. 16 the end-effector is made of four parts: (1) a flat frame

bearing spherical markers (3), the alignment cylinder (2) and a cap (4) which allows the surgeon to adjust the friction by which the needle is held in position. In particular, the lower section of the cap (Fig. 16) is locked in alignment cylinder, and it hosts a seal, which can be compressed by three screws positioned at 120° with respect to each other. Tightening the screws increases the friction, allowing the surgeon to block the needle at a defined depth into the cylinder, while, untightening the screws allows changing the needle or guiding it during insertion.

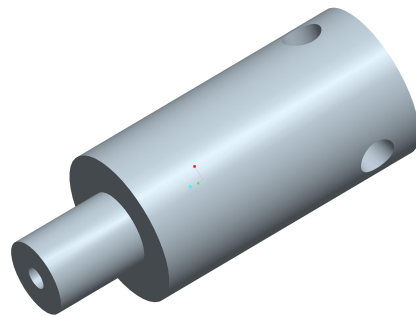


**Figure 17: Needle's cap for friction adjustment**

## **2.4 Electronic Control**

Electronic control system is designed as a master-multi slaves chain of microprocessors. The robot arm is equipped with six microcontrollers, one per joint, working as a slave, plus one that works as a master for the chain. The master of the chain is used also to interface the robot with the computer, using USB2 connection. The connection between microprocessor is serial (bus I2C) and a series of buffers are used in order to increase the communication speed. The bus frequency is 400 KHz. This bus frequency allows communicating with all slaves, using a 4 byte frames format, in 1.6ms. Currently, the user controls the equipment with an application developed in Matlab for Windows, through ad hoc routines written in C++, which makes the system extremely simple to work with. The current software can require from each joint controller the

actual value of the encoder's angle (all values are recorded at the same time using a general call). It also can open or lock one the brakes, or it can require reaching the specified angle from the current value, in a given time, starting from a second general command that starts the motion of all joints. Each controller then calculates its ramps of acceleration and deceleration.

## 2.5 Braking System Design

The brake system prototype developed for the robotic system, as shown in the CAD model below, is a drum brake working as a switch on/off and whose brake shoes are placed in contact with the housing by the rotation of two cams.

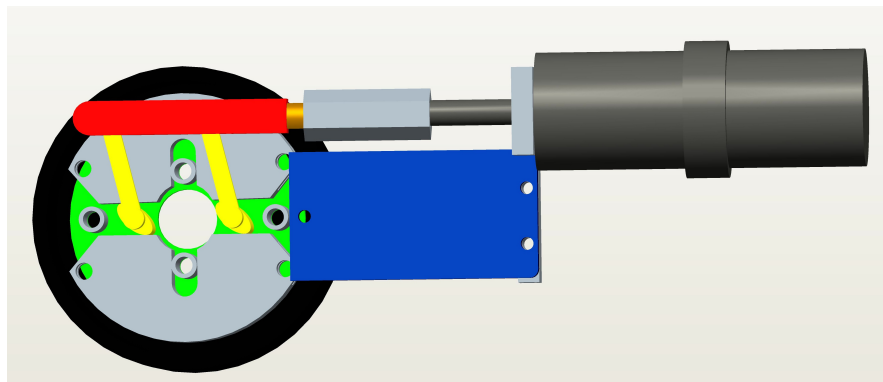


**Figure 18: brake system unlocked position**

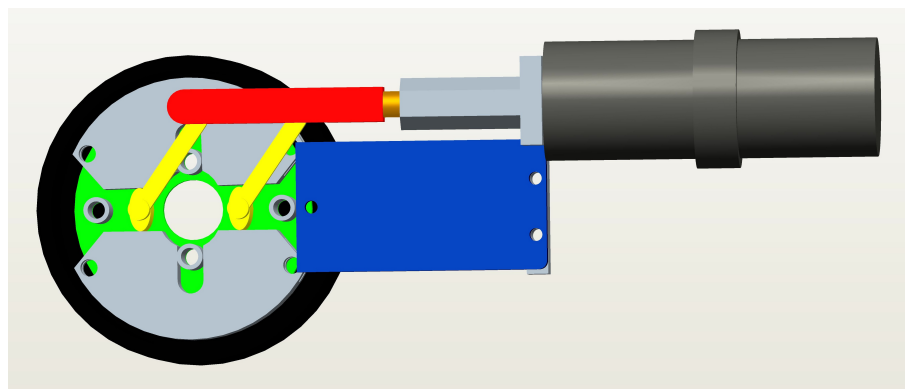


**Figure 19: brake system locked position**

The frame and cover are provided by a central hole for the shaft on which the

housing of the brake is rigidly linked. Pulling the slider, the cams rotate, opening the brake shoes outwards. In this configuration (“locked position” Fig. 19) brake shoes and housing come in contact each other and the friction avoid the relative motion between the housing, hence the shaft as well, and the frame. When the slider is pushed inside, the brake shoes helped by two springs (shown in Fig. 20) come back in the previous configuration (“unlocked position” Fig. 18) unlocking the shaft. The cams are guided by two supports belonging to the frame, allowing linking a cover, which keeps all the components in place. The slider instead, is linked to a sleeve rigidly attached to a shaft of a motor-reducer, which control the locking mechanism of the brake whose actual picture can be seen below.

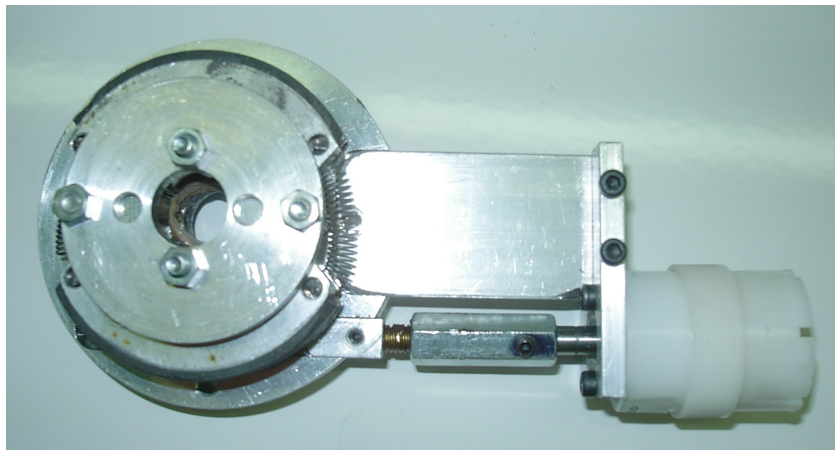


**Figure 20: Brake system assembly prototype**

The control strategy adopted for activating/deactivating the braking devices is based on the measure of the current absorbed by the electric actuator, i.e. the revolutive motor. Calibrating the device, the maximum current absorbed by the motors to brake/release each joint is registered. A lower value, higher than the value registered during the activating phase, is hence used as a threshold in the control algorithm, which stops the input power supply when the current overtakes this limit. As an indication, Fig 21 shows a graph of the current absorbed by the motor (DC Johnson 3F2212), when braking, as a function of

time. To unlock, the motor rotation is inverted, and operated for a second, more than enough to free the drum.

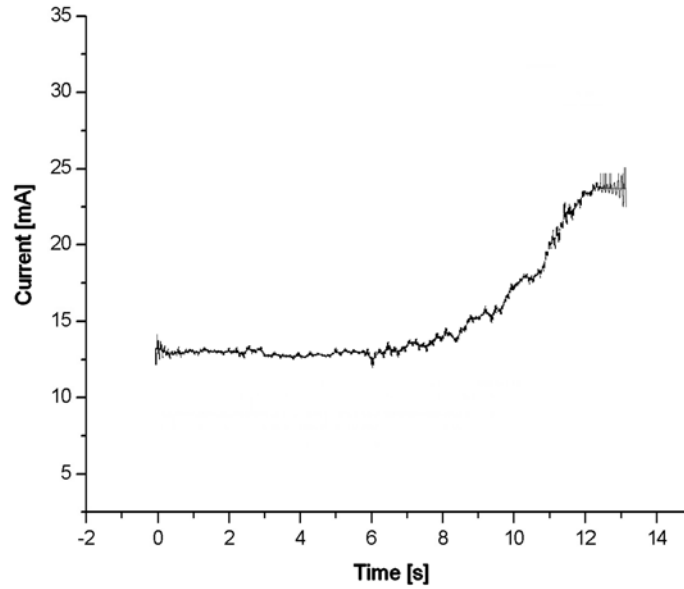


Figure 21: Braking current load

## 2.6 Brake Theoretical Analysis

In this paragraph, a theoretical analysis of the geometry of the brake shoes including the brake lining (friction material) is reported. The goal of this analysis is to study the locking condition as function of the brake shoes opening angle  $\theta$ . According to Reys' theory, the volume of the material removed by friction is proportional to the work of friction or rather:

$$dV = K \cdot dL \quad [18]$$

In terms of superficial contact we can state the following equation:

$$dA \cdot \delta \cdot \Delta t = K \cdot f \cdot p \cdot dA \cdot v_p^r \cdot \Delta t \quad [19]$$



with  $dA$  area of the element subject to wear,  $f$  is friction's coefficient between the materials in contact,  $\delta$  is the thickness of wear debris along the normal direction to the area  $dA$ ,  $K$  is a proportional (or wear coefficient),  $p$  is the contact's pressure,  $\Delta t$  is the time interval and  $v_p^r$  is the relative velocity for a generic point between two bodies in contact (Fig. 22) . Thus, the pressure's contact value can be evaluated as:

$$p = \frac{\delta}{K \cdot f \cdot v_p^r} = \frac{\delta}{K \cdot f \cdot \omega \cdot R} \quad [20]$$

Therefore, known the relative velocity, being  $K$  a constant, the pressure can change according to a law similar to the one, which state for the wear debris. This law is also related to the type of motion's approach between the surfaces in contact. Since the brake shoes approach the drum by translating along their axis of symmetry we can assert that the thickness of the wear debris changes as function of an angle  $\theta$  according to:

$$\delta = \delta_0 \cos\theta \quad [21]$$

thus if  $\theta$  is zero the thickness is maximum. Such condition is verified in middle of the brake shoe along its axes of symmetry.

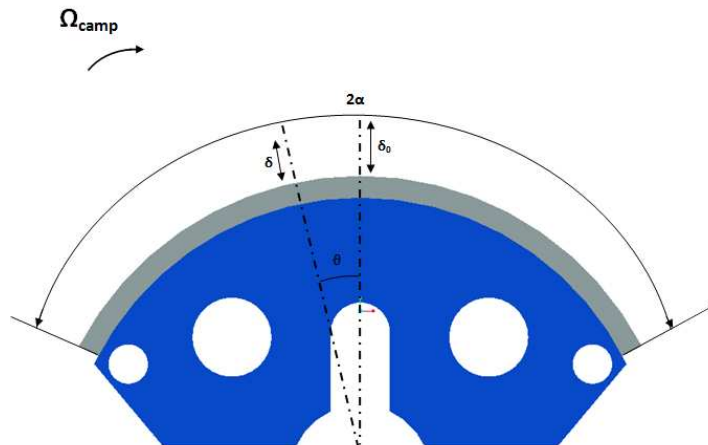
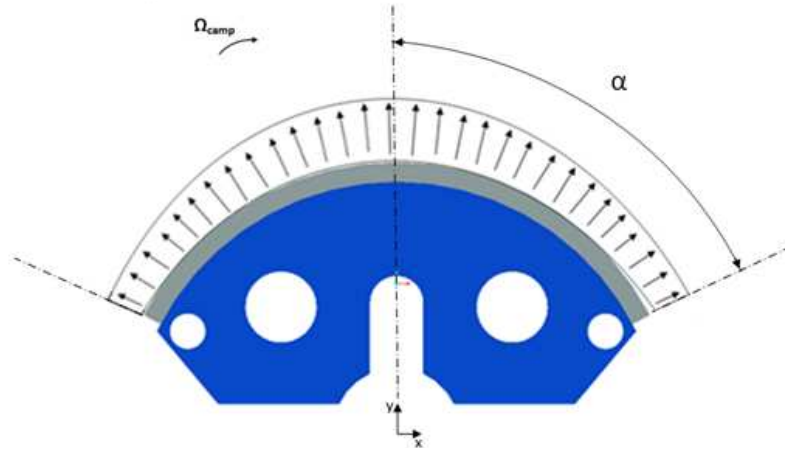


Figure 22: Brake's shoe geometry



**Figure 23: Brake's shoe pressure load**

the pressure will change according to:

$$p = \frac{\delta_0 \cos \theta}{K \cdot f \cdot \omega \cdot R} = p_0 \cos \theta \quad [22]$$

therefore, the pressure reaches the maximum along the line of approach between housing and brake's shoe. The total pressure on the horizontal direction is zero, since the forces on the right side compensate the forces on the left side. Instead the modulus of the sum of the forces on y direction can be calculated integrating the vertical components of pressure along the whole arch of the shoe:

$$F_p = \int_{-\alpha}^{\alpha} p \cdot s \cdot R \cdot \cos \theta \cdot d\theta = p \cdot s \cdot R \int_{-\alpha}^{\alpha} \cos^2 \theta \cdot d\theta \quad [23]$$

$$F_p = p \cdot s \cdot R \cdot \left( \alpha + \frac{1}{2} \sin 2\alpha \right) \quad [24]$$

where s is thickness of the brake shoe. The friction that determines the brake torque directly depends on pressure on the brake shoe and of course it is

tangent to the contact's surface. Symmetrically the total friction on the y direction is zero (Fig. 23), while it is not null on the x direction, imposing the brake torque from the brake shoe to the housing. This torque is generated by the tangential component  $F_t$  and can be expressed as:

$$F_t = \int_{-\alpha}^{\alpha} p \cdot s \cdot R \cdot \cos\theta \cdot d\theta = f \cdot p_0 \cdot s \cdot R \cdot \left( \alpha + \frac{1}{2} \sin 2\alpha \right) \quad [25]$$

therefore the total brake torque can be written as follow:

$$M_f = 2f \cdot p_0 \cdot s \cdot R^2 \cdot \sin\alpha \quad [26]$$

We need to determine where the point of application of the force  $F_t$  is located, or rather the length of the lever-arm  $d$ . To do so, we can state the following:

$$M_f = F_t \cdot d \quad [27]$$

thus, replacing the values of  $F_t$  and  $M_f$  with the respective equations previously deduced we have:

$$d = \frac{1}{2} M_f \frac{1}{F_t} = R \frac{\int_{-\alpha}^{\alpha} p \cos\theta \cdot d\theta}{\int_{-\alpha}^{\alpha} p \cos^2\theta \cdot d\theta} = R \frac{2\sin\alpha}{\alpha + \frac{1}{2} \sin 2\alpha} \quad [28]$$

Since  $\cos^2\theta < \cos\theta$  follows that  $d$  is greater than the radius  $R$  and thus the total force which causes the brake torque is applied to a greater distance than the radius of the brake shoe.

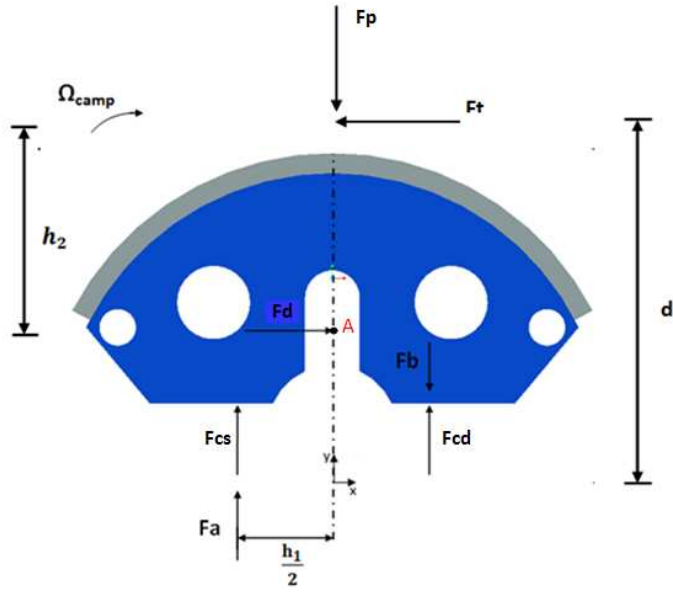


Figure 24: Brake's shoe static equilibrium

Now we are going to state the static equations for a brake shoe considering the actions of the cams in the free body diagram reported in Fig. 24. Indicating with:  $F'_{cs} = F_{cs} + F_a$  and  $F'_{cd} = F_{cd} + F_b$  the conditions of static equilibrium are:

$$F_t = F_d \quad [29]$$

$$F'_{cs} + F'_{cd} = F_p \quad [29]$$

$$F_t \cdot h_2 + F'_{cd} \cdot \frac{h_1}{2} - F'_{cs} \cdot \frac{h_1}{2} = 0 \quad [30]$$

being  $F_t = fF_p$  the following equation can be derived:

$$F_t = \frac{M_F}{d} \quad [31]$$

$$F'_{cd} = \frac{M_f}{d} \left( \frac{1}{2f} - \frac{h_2}{h_1} \right) \quad [32]$$

The locking condition is reached when  $F_b$  (directed as shown in Fig. 24) is greater or equal to  $F_{cd}$  which means that  $F'_{cd}$  has the same direction of  $F_b$ . Therefore, to reach this condition must be verified the following:

$$f > \frac{h_1}{2h_2} \quad [33]$$

thus, to make sure the brake is able to self-lock we need to reduce the distance  $h_1$  by getting close the cams to the axis of symmetry or we need to increase the arch of the brake shoes.

## 2.7 Numerical Simulations and Testing

In order to validate the model and calculate the maximum value of the brake torque for the braking system prototype, multi-body simulations and an experiential test were performed. Below a CAD model of the braking system used in the simulations, with and without the housing, is shown in Fig 25.

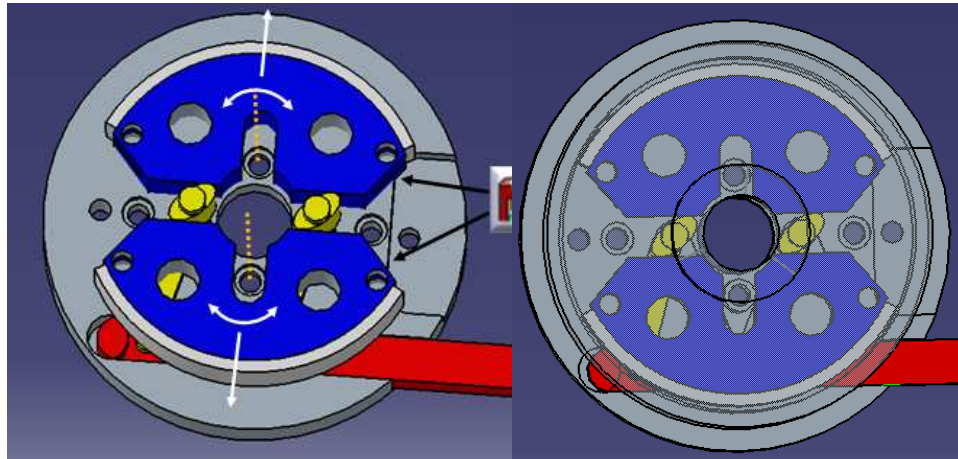


Figure 25: Brake system multi-body cad model

First, the force applied to the slider has been calculated knowing the technical specification of the dc motor and the screw linked to slider.

The torque supplied by the dc motor is 0.5 Nm, while the screw selected was a metric six, pitch 1. The force applied to the slider can be calculated as follows:

$$F_s = \frac{2000 \cdot \pi \cdot \eta_v \cdot C_m}{p} \quad [34]$$

where:  $\eta_v$  is the efficiency of the screw,  $C_m$  is the torque supplied by the motor,  $p$  is the pitch. The value found for the force applied to the slider was about 300N. Using this value and setting proper constraints for the friction between the components, a variable loading torque was applied to the housing starting from 5Nm. The maximum load found were about 20Nm, over this value, the housing's velocity is greater than zero, since the friction between housing and brake shoes is no longer sufficient to stop the motion of the housing.

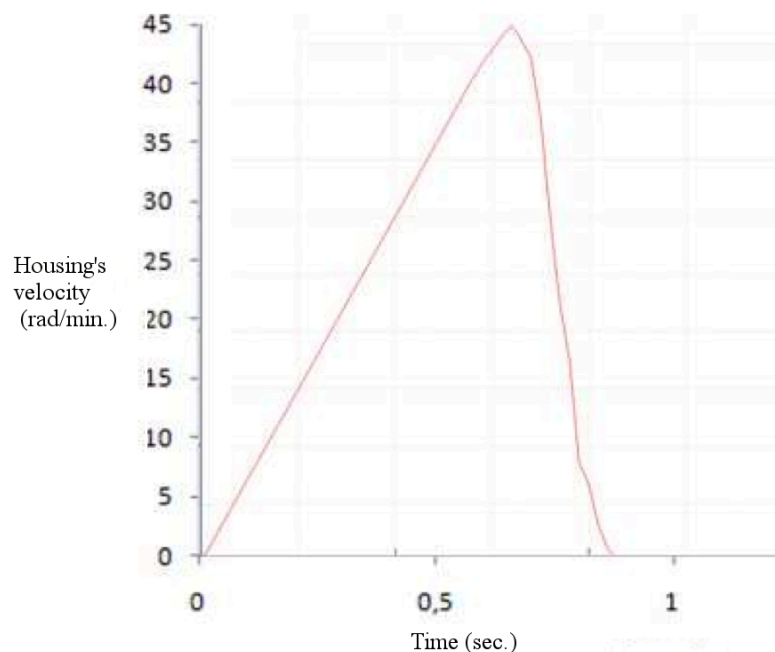


**Figure 26: Housing's velocity during braking**

As shown in Fig. 26, the velocity of the housing increases until the contact between brake shoes and housing starts, thus it goes rapidly to zero.

Finally, an experimental test was performed (Fig. 27). To do so, a special housing bearing a nut was manufactured and the brake was mounted on a joint of the Navi-Robot. Hence, the brake was locked and by using a dynamometric torque wrench, increasing values of torque were imposed to the housing. The maximum value which the brake was able to support was about 19 Nm similar to the one found by dynamic simulations. Over this value the friction was no

longer sufficient to avoid the rotation of the housing, but no structural damages were noticed with the internal brake's components.



**Figure 27: Brake system experimental test**

## **2.8 Navi-Robot Calibration**

Once the brake system was tested, a set of 12 brakes (2 per joint) was manufactured and assembled on the joints of the robot. The final structure of the robot is shown in Fig.28.

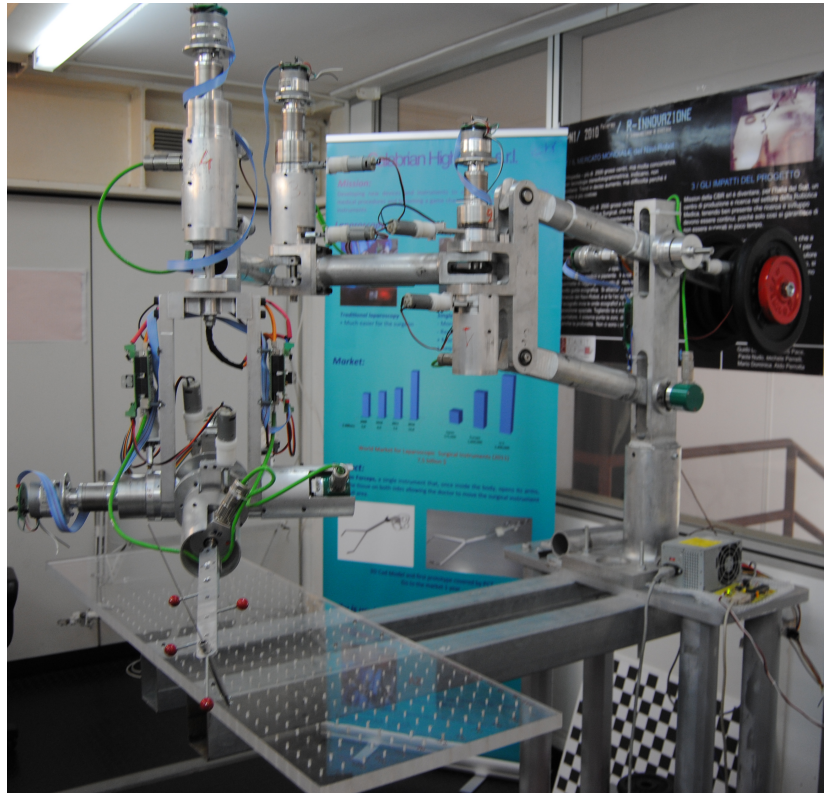


**Figure 28: Navi-Robot prototype**

The final position accuracy of the robot is mainly influenced by: kinematic inaccuracy (due to manufacturing and assembly errors in both actuated and passive joints), load deformation (due to external forces including gravity) and thermal deformation. One possibility to compensate for geometrical errors is to perform a kinematic calibration. The robot is requested to reach some desired poses and the reached actual poses are measured. Then, the exact robot geometry is estimated analyzing the difference between the desired and the reached poses. This procedure requires a parametric identification of the manipulator, which consists in the formulation of a geometrical model of the robot in which each source of error is represented by a parameter. The parameter set includes link lengths, joint axes inclination and joint coordinate offsets.

Using the model described in paragraph 2 (Fig. 12), the robot was forced to



reach a set of predefined known poses, and for each of them, the corresponding joint rotation was measured. For this purpose, a particular end-effector was manufactured by a CNC machine and rigidly connected to the last link of the robot (link 6). The terminal element of the link is a shaft, which was provided by a hole (end-effector-robot connection point). The shaft first, is inserted in the end-effector connection tube and then fixed to it by means of a screw. (Fig.29). The terminal element of the calibration end-effector is a cube, on three faces of it, are placed 12 pins, equally spaced. The axis of the end-effector connection tube passes through the center of the cube, defining three different angles with respect to each face provided by pins.

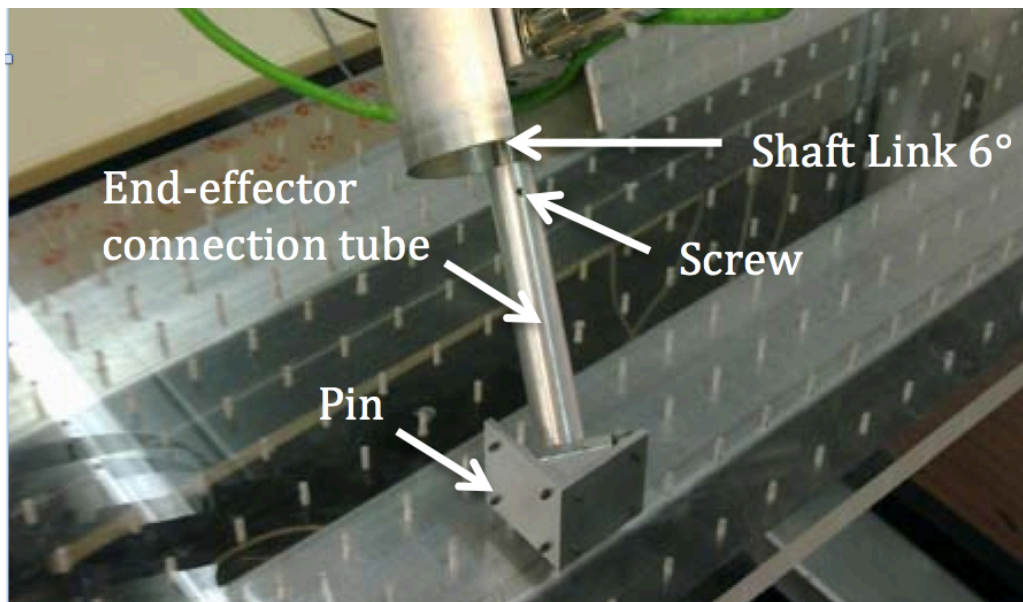


**Figure 29: Navi-Robot calibration setup**

The end-effector was designed to be placed in different known positions on a Plexiglas board provided by a series of holes on its surface. In particular, each 4-pins set of the cube can fit in 4 holes of the board forcing the robot to assume a different joints' configuration for each face of the cube in contact with the board. Hence, during the calibration procedure, several poses of the end-effector were collected, registering the angles of the joints. These values are

recorded together with the correspondent theoretic end-effector pose position. To improve the calibration accuracy and to cover the whole working area with different end-effector orientation the measuring board was designed to have 360 insertion holes within the robot workspace.

The calibration procedure was performed as follows: 180 poses were collected, for each of one, we evaluated the distance between the known end-effector positions with those estimated using the measured joint rotations and the evaluated structural parameter errors. The average position error before calibration procedure was about 4.1 mm with standard deviation of 7.3 mm and 11.1 mm as maximum value. After the calibration average position error was -0.02 mm with a standard deviation of 0.3 mm and 0.9 mm as maximum value.

In order to perform the biopsy the end-effector used for the calibration was replaced by the end-effector bearing the needle and the marker described in section 2.3. Since even this end-effector is affected by geometric error due to manufacturing errors, a calibration procedure is required to compensate these errors by calculating a set of six error parameters denoting the end-effector geometry. Using a similar procedure to that previously described, the tip of the needle was placed in known positions and we evaluated the distance between the known needle positions with those estimated using the measured joint rotations and the evaluated structural parameter errors. The average position error was 0.05 mm with standard deviation of 0.4 mm and 1.3 mm as maximum value. According to a definition from international standards (ISO 9283), we estimated the robot repeatability as  $d + 3\sigma = \pm 0.4$  mm.

### **3. Computer Vision Theory**

An important outcome of the project was to integrate the Navi-Robot with a C-arm fluoroscopy system setup. In this thesis however, due to the difficulty to source it, for experimentation, the fluoroscope was simulated using a digital camera. This requires the assumption that a fluoroscopy system, even though

quite different in physical appearance and image capturing method, can be described by the defined camera model used in the project, using the vision theory described below. The camera model, as well as the theory regarding lens distortion, calibration and triangulation, will be addressed. Image processing techniques used will also be elaborated on.

The theory described is primarily contained in detail in the book Multiple View Geometry in Computer Vision by Hartley and Zisserman [32].

In this section, the concept of the camera projection matrix and the information contained within it is explained. The method of calculation and the implementation of the camera matrix in calibrating a camera and finally reconstructing 3D points from a pair of 2D images will be shown.

### 3.1 The Camera Projection Matrix

Simply stated, the mathematical relationship between points in a 2D image and the corresponding points of a 3D object is described by the camera projection matrix ( $\mathbf{P}$ ), which can mathematically be described as:

$$x = PX \quad [35]$$

where  $x$  is a homogeneous 3-vector  $(x, y, 1)^T$ , which is the pixel in the 2D image,  $P$  is the 3 x 4 camera projection matrix and  $X$  is a world coordinate in 3D represented by a homogeneous 4-vector  $(X, Y, Z, 1)^T$ . The camera projection matrix  $\mathbf{P}$  contains two pieces of invaluable information: (a) The intrinsic or internal parameters ( $\mathbf{K}$ ) of the camera and (b) the extrinsic or external parameters of the camera which include the camera rotation ( $\mathbf{R}$ ) and translation matrix ( $\mathbf{t}$ ), as well as the position of the camera center ( $\mathbf{C}$ ). These matrices and their origin will be explained in the subsequent sections.

The simplest transformation, the 2D homography as described by Hartley and Zisserman, is stated as follows:

Given a set of points  $x^i$  in  $P$  (the 2D projection plane) and a corresponding set of points  $x'_i$  likewise in  $P_2$ , compute the projective transformation that takes each  $x_i$  to  $x'_i$ . The 3D to 2D case will be considered hereafter.

## 3.2 2D to 2D Case

Considering a set of point correspondences  $x_i \leftrightarrow x'_i$  between two images, the problem is to compute a 3 x 3 matrix  $H$  such that  $x_i H = x'_i$  for each  $i$ . There will be a minimum number of point correspondences needed to compute  $H$ . The matrix  $H$  contains nine entries, but is defined only up to scale. The number of degrees of freedom in a 2D projective transformation is eight. Each point-to-point correspondence also accounts for two constraints, since for each  $x_i$  in the first image the two degrees of freedom of the point in the second image must correspond to the mapped point  $x_i H$ . A 2D point has two degrees of freedom corresponding to the x and y components, each of which may be specified separately. Alternatively, the point is specified as a homogenous 3-vector, which also has two degrees of freedom since scale is arbitrary. It is thus necessary to specify four point correspondences in order to constrain  $H$  fully for the 2D to 2D case.

## 3.3 The Direct Linear Transform Method (DLT)

The Direct Linear Transformation, or DLT, is the simplest linear algorithm for computing from  $H$  four 2D to 2D homogeneous point correspondences. The DLT method is also utilized in other algorithms used in this thesis. Prior to using the DLT method, an important step called data normalization, is performed which entails translation and scaling of image coordinates. Apart from improving accuracy results, data normalization also makes the algorithm

incorporating the normalization step invariant with respect to arbitrary choices of scale and coordinate origin. The normalization method, in short, comprises the following three steps:

1. The specified points are translated so that their centroids are situated at the origin
2. The specified points are scaled so that the average distance from the origin is  $\sqrt{2}$ , meaning that the average point is at  $(1,1,1)^T$
3. The transformation is applied to the two images separately :

$x_i \mathbf{H} = x'_i$  can be expressed in terms of the vector cross product as  $x'_i \times x_i \mathbf{H} =$

0. Now writing the  $j^{\text{th}}$  row of the H-matrix as  $\mathbf{h}^{jT}$ , then

$$Hx_i = \begin{pmatrix} h^{1T} x_i \\ h^{2T} x_i \\ h^{3T} x_i \end{pmatrix} \quad [36]$$

The vector cross product, where  $x_i = (x'_i, y'_i, w'_i)^T$ , with  $w_i w'_i = 1$  (homogenous coordinates), can now be shown to be

$$x_i \times Hx_i = \begin{pmatrix} y'_i h^{3T} x_i - w'_i h^{2T} x_i \\ w'_i h^{1T} x_i - x'_i h^{3T} x_i \\ x'_i h^{2T} x_i - y'_i h^{1T} x_i \end{pmatrix} \quad [37]$$

Substituting  $h^{jT} x_i = x'_i h^j$  in equation 37 for j-values 1, 2 and 3 produces the following:

$$\begin{bmatrix} 0^T & -w'_i x_i^T & y'_i x_i^T \\ w'_i x_i^T & 0^T & -x'_i x_i^T \\ -y'_i x_i^T & -x'_i x_i^T & 0^T \end{bmatrix} \begin{pmatrix} h^1 \\ h^2 \\ h^3 \end{pmatrix} = 0 \quad [38]$$

Now since the above equation is of the form  $A_i h = 0$ ,  $h$ , is a 9-vector made up of  $h_i$  with  $i = 1, 2, \dots, 9$  and a matrix as shown in equation 39:

$$A = \begin{bmatrix} 0^T & -w'_i x'_i{}^T & y'_i x'_i{}^T \\ w'_i x'_i{}^T & 0^T & -x'_i x'_i{}^T \\ -y'_i x'_i{}^T & -x'_i x'_i{}^T & 0^T \end{bmatrix}, h = \begin{pmatrix} h^1 \\ h^2 \\ h^3 \end{pmatrix}, H = \begin{bmatrix} h_1 & h_2 & h_3 \\ h_4 & h_5 & h_6 \\ h_7 & h_8 & h_9 \end{bmatrix} \quad [39]$$

Equation 39 can be simplified to

$$\begin{bmatrix} 0^T & -w'_i x'_i{}^T & y'_i x'_i{}^T \\ w'_i x'_i{}^T & 0^T & -x'_i x'_i{}^T \end{bmatrix} \begin{pmatrix} h^1 \\ h^2 \\ h^3 \end{pmatrix} = 0 \quad [40]$$

as only, two of the three equations in  $A$  are linearly independent. The third row is the sum of the first two equations with a scaling factor. If we have the minimum of four corresponding points, we obtain the equation  $A \mathbf{h} = 0$  by stacking each to form  $A$ . The matrix  $A$  has rank eight, and thus has a 1-dimensional null-space, which provides a non-zero solution for  $\mathbf{h}$ . The solution can only be determined up to a non-zero scale factor, but  $H$  is normally only determined up to scale. The solution  $\mathbf{h}$  gives the required  $H$  with a scale for the vector chosen. In practice, the measurements of image points are not exact due to noise. If more than four point correspondences are given with the presence of noise, the system is over-determined and the solution will not be exact. By minimizing some cost function it was attempted to find the best possible approximation for the vector  $h$ . The singular value decomposition (SVD) is a matrix decomposition technique commonly used for the solution of over-determined systems of equations. The solution is the unit singular vector corresponding to the smallest singular value of  $A$ .

### 3.4 3D to 2D Case

For finding the transformation of 3D to 2D points, the same theory is applicable. Normalization is again a prerequisite. The only difference compared to the 2D to 2D case is that the points are scaled so that the distance from the origin is equal to  $\sqrt{3}$ , or on average  $(1, 1, 1)^T$ . Again we need to find a camera matrix  $P$ , now a  $3 \times 4$  matrix such that  $x_i = P X'_i$  for all  $i$  where  $x_i$  is the 2D

image coordinates and  $X_i$  are the 3D coordinates. The difference is the dimension of the  $P$ -matrix, which in this case is a  $3 \times 4$  and not a  $3 \times 3$  matrix. Similar to the 2D to 2D case, the relationship between  $X$  and  $x$  is:

$$\begin{bmatrix} 0^T & -w'_i x_i^T & y'_i x_i^T \\ w'_i x_i^T & 0^T & -x'_i x_i^T \\ -y'_i x_i^T & -x'_i x_i^T & 0^T \end{bmatrix} \begin{pmatrix} P^1 \\ P^2 \\ P^3 \end{pmatrix} = 0 \quad [41]$$

where the 4-vector  $P^{iT}$  is the  $i^{\text{th}}$  row of matrix explained in the 2D to 2D case, the last row of the  $A$ -matrix can be left out leaving only

$$\begin{bmatrix} 0^T & -w'_i x_i^T & y'_i x_i^T \\ w'_i x_i^T & 0^T & -x'_i x_i^T \end{bmatrix} \begin{pmatrix} P^1 \\ P^2 \\ P^3 \end{pmatrix} = 0 \quad [42]$$

The  $A$ -matrix is of the form  $2n \times 12$ , where  $n$  is the number of point correspondences.  $P$  can now be calculated by solving  $Ap = 0$  where  $p$  is the vector containing the entries of matrix. The minimum number of point correspondences needed for this case is  $5\frac{1}{2} \cong 6$  points as the matrix  $P$  has 11 degrees of freedom and two equations are obtained per point pair. Similar to the 2D case, the  $P$ -matrix is calculated implementing the SVD.

### 3.5 The Camera Model

As mentioned in the previous section, the camera matrix provides information regarding the intrinsic as well as extrinsic parameters of a camera. In this section, the basic pinhole camera model, used as the starting point for developing most camera models, will be explained. The CCD camera model used in this project is a camera model with additions to the normal pinhole model. Explanations contained in this section are described in detail by Hartley and Zisserman [32]. Lens distortion plays an important role in the accuracy of 3D point reconstruction and needs to be taken into account in the model. The

final camera model used will thus have to consider distortion in the model.

### 3.6 Basic Pinhole Camera Model

The basic pinhole camera is the simplest of the camera models and is used commonly as first assumption when applying camera calibration methods. In this model, illustrated in Fig. 30, a point in space with coordinates  $X = (X, Y, Z)^T$  is mapped to a point on the image plane at  $x$  (distance  $f$ ), where the line joining the point to  $X$  the center of the projection meets the image plane. We can see that the point  $(X, Y, Z)^T$  can be mapped to  $(fX/Z, fY/z, f)^T$  on the image plane. Some definitions: the line from the camera center ( $C$ ), which is the center of projection, perpendicular to the image plane, is called the principle axis. The point on the image plane is called the principle point ( $p$ ).

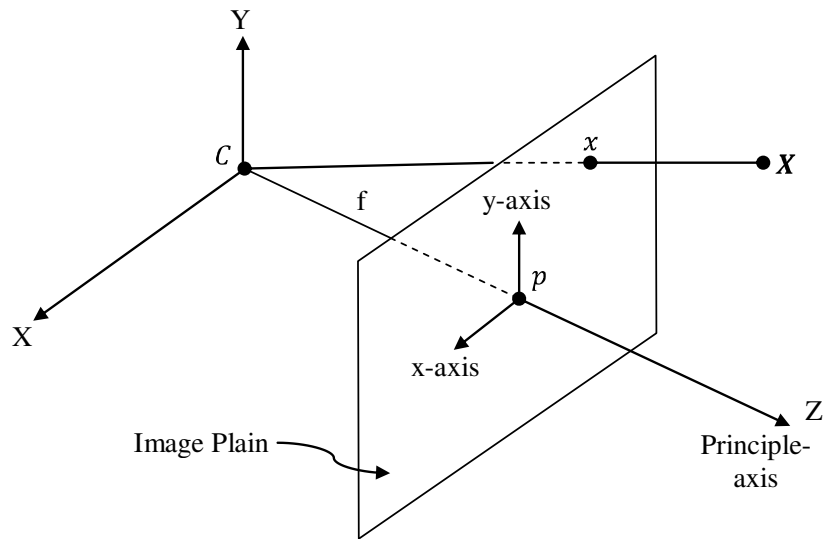


**Figure 30: Basic pinhole camera model**

Central projection is represented using homogenous vectors. World and image coordinates can be related by a linear mapping written as:



$$\begin{pmatrix} X \\ Y \\ Z \\ 1 \end{pmatrix} \rightarrow \begin{pmatrix} fX \\ fY \\ Z \end{pmatrix} = \begin{bmatrix} f & & 0 \\ & f & 0 \\ & & 1 \end{bmatrix} \begin{pmatrix} X \\ Y \\ Z \\ 1 \end{pmatrix} \quad [43]$$

Writing equation 43 compactly where the world point  $x$  is  $(X, Y, Z, 1)^T$  and the image point  $x$  is  $(X, Y, 1)^T$  the following equation results:

$$x = PX \quad [44]$$

where  $P$  is the camera projection matrix. If the principle point is not at the center of the image, this is taken into account by placing the principle point coordinates  $(p_x, p_y)^T$  in the  $P$ -matrix as shown in equation 45:

$$\begin{pmatrix} X \\ Y \\ Z \\ 1 \end{pmatrix} \rightarrow \begin{pmatrix} fX + Zp_x \\ fY + Zp_y \\ Z \end{pmatrix} = \begin{bmatrix} f & & p_x & 0 \\ & f & p_y & 0 \\ & & f & 0 \end{bmatrix} \begin{pmatrix} X \\ Y \\ Z \\ 1 \end{pmatrix} \quad [45]$$

The matrix  $K$ , called the camera calibration matrix, is the matrix containing the intrinsic parameters of the camera.

$$K = \begin{bmatrix} f & & p_x & 0 \\ & f & p_y & 0 \\ & & f & 0 \end{bmatrix} \quad [46]$$

Writing equation 46 in concise form results in

$$x = K[I|0]X_{cam} \quad [47]$$

where  $(X, Y, Z, 1)^T$  is written as  $X_{cam}$  to show that it is assumed to be located at the origin of the Euclidian coordinate system with the principle axis pointing

down the  $z$ -axis. The world and camera coordinate frames are related by a translation and rotation, which was earlier noted to be the extrinsic parameters of the camera. 3D points are usually described in the world coordinate system, and are then translated to the camera coordinate system. It is no different in this project. If a 3D point is known in the world coordinate frame, it can be written in the camera coordinate frame as

$$x = KR[I] - \tilde{C}]X \quad [48]$$

where  $R$  and  $C$  are the parameters related to the camera rotation and center respectively.

### 3.7 Epipolar Geometry

In this section the basic stereovision principles are explained to better understand the reconstruction of 3D coordinates from 2D images. Epipolar geometry, as well as the fundamental matrix, will be covered. Triangulation is also briefly discussed. Simply stated, epipolar geometry is the intrinsic projective geometry between two views of the same object or scene.

This geometry depends only on the cameras internal parameters and the relative orientations thereof. Epipolar geometry is in most cases motivated by considering the search for corresponding points in a stereo image pair. It is no different in this project. Using the notation from Hartley and Zisserman [32], points with an apostrophe (‘) corresponds with the second image and points without to the first image [32].

When a point  $X$  is imaged in two views, with  $x$  in the first view and  $x'$ , in the second, the geometry can be visualized as shown in Figure 31. This represents a typical stereovision setup.  $C$  and  $C'$  refer to the center points of the two respective cameras. The line connecting the two camera centers is called the baseline. The baseline intersects the first and second image plane at two points; and  $e'$ , for the two image planes respectively. These intersecting points are called the epipoles. As shown in Fig. 31, the point  $X$ ,  $x$ ,  $x'$ , and are coplanar

which means that a plane can be fitted through the points. This plane is depicted in Fig. 31 by  $\pi$ .

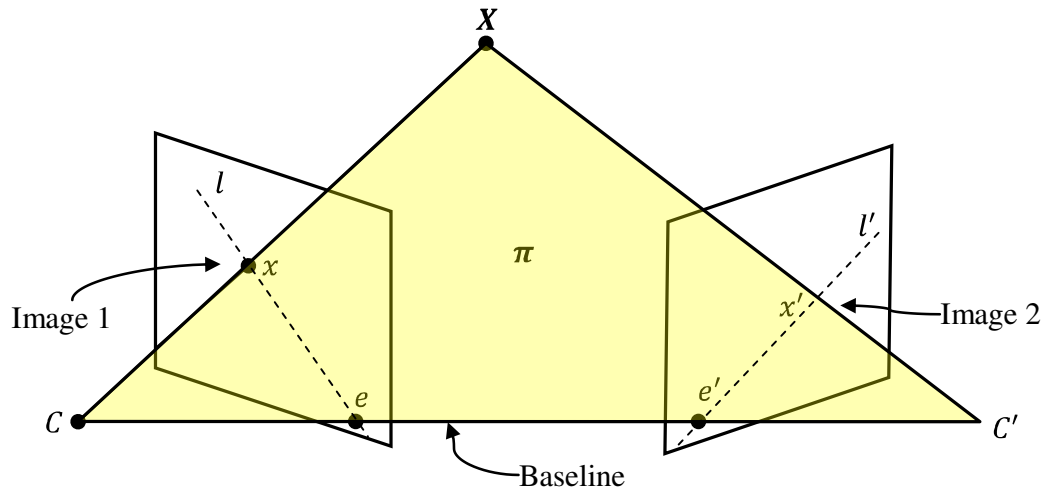


Figure 31: Epipolar geometry

This property that the back-projected rays from the two points on the image plane to the 3D point all lie in the plane  $\pi$ , introduces a method by which a point correspondence search can be aided.

The plane  $\pi$  can be defined by the baseline and the ray defined by  $x$ . From the above explanation, it is known that the corresponding point  $x$ , lies in the plane  $\pi$ . This means that  $x'$  lies somewhere on the intersecting line of the plane  $\pi$  and the second image plane. This line is denoted as  $l'$ , and is in effect the view of the ray of  $x$  back-projected onto the second image plane. The line  $l'$  is called the epiline of  $x$ . In the same manner, an epiline  $l$  of  $x$  is shown on the first image plane. The epiline thus allows the search for point correspondences to be narrowed only to a line on an image. As the project entailed the reconstruction of corresponding points chosen by the surgeon on an image pair, a method was needed to improve point selection accuracy. This was provided by the characteristics of epipolar geometry. A matrix, called the fundamental matrix, was crucial in its application.

### 3.8 Fundamental Matrix

The fundamental matrix describes the relationship between two cameras and is the basis on which stereovision is built. The fundamental matrix is the unique  $3 \times 3$  homogeneous matrix of rank 2 that satisfies the following:

$$x^T F = x'^T \quad [49]$$

And

$$x'^T F = x^T \quad [50]$$

for all corresponding points  $x \leftrightarrow x'$ . It is thus a compact algebraic representation of the epipolar geometry of two images. As explained in the description of epipolar geometry, this characteristic is of great importance as the search for the point correspondence of a point chosen in the first image is narrowed to a line, the epilines, crossing the second image. Different methods exist to compute the fundamental matrix. The best solution depends on the information available. As the camera matrices of the stereo setup have been obtained ( $P$  and  $P'$ ) a method using these two pieces of information was implemented. With the two camera matrices known, the ray back-projected from  $x$  by  $P$  is obtained by solving  $PX = x$ . The one-parameter family of solutions is then given by:

$$X(\lambda) = P^+x + \lambda\tilde{C} \quad [51]$$

where  $P^+$  is the pseudo-inverse of  $P$ , i.e.  $PP^+ = I$  where  $I$  is the identity matrix, and  $\tilde{C}$  is the camera center. Two points of interest on the ray are  $P^+x$  (at  $\lambda = 0$ ) and the camera center (at  $\lambda = \infty$ ). These two points are imaged by the second camera  $P'$  as  $P'P^+x$  and  $P'\tilde{C}$  respectively. The epipolar line is the line joining these two projected points, namely

$$l' = (P'\tilde{C}) \times (P'P^+x) \quad [52]$$

The point  $P'\tilde{C}$  is the epipole in the second image and is denoted by  $e'$ . Thus:

$$l' = [e'] \times (P'P^+x) = Fx \quad [53]$$

where  $F$  is the matrix

$$F = [e'] \times P'P^+ \quad [54]$$

The matrix  $F$  computed by this method must satisfy the condition that for any pair  $x \leftrightarrow x'$  of corresponding points in the two images, equation 55 is satisfied.

$$x'Fx = 0 \quad [55]$$

### 3.9 Triangulation

Triangulation is the process of reconstructing a point in 3D by two rays that intersect at that point. In the case of perfect calibration and point extraction, the rays from the image pair will intersect. This is not the case in practice due to the inaccuracies of calibration. Linear and non-linear techniques are described to solve this problem. The DLT method used in obtaining the camera projection matrix is again used during the process of triangulation. The triangulation method implemented is described by Hartley and Zisserman [32].

## 4. Fluoroscopy Based Biopsy

This chapter gives an overview of the main components of the system, as well the working principle, which allows integrating a single camera simulating a C-arm fluoroscopy system with the robotic system in order to guide a precision biopsy. The imaging systems, as well the calibration procedure, the end-effector carrying the needle and the software are described.

## 4.1 C-Arm Fluoroscopy System Overview

The components included in a modern fluoroscopic imaging system are shown in Fig. 32. Some components are similar to those included in systems used exclusively for radiography, whereas others are unique to fluoroscopy. Typically, additional apparatus are attached to allow for image recording, such as a spot-film device, film changer, photo-spot camera, cine camera, or analog-to-digital converter.

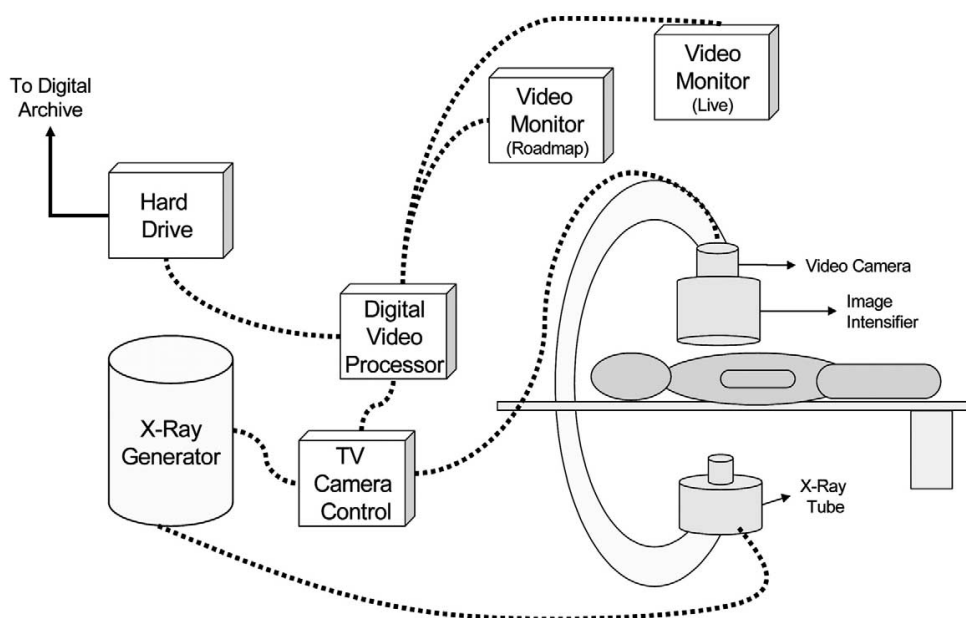
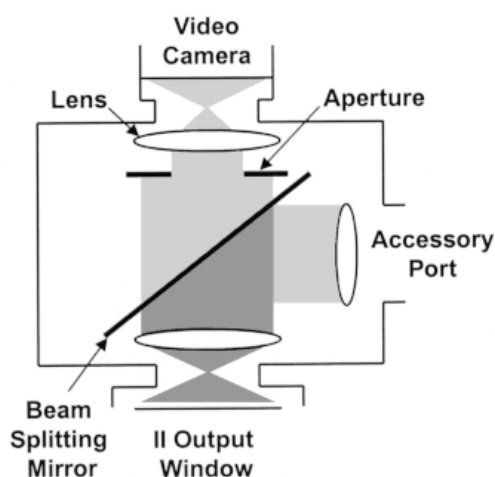


Figure 32: C-arm fluoroscopy system's elements

The x-ray generator allows selection of kilovolt peak (kVp) and tube current (mA) that is delivered to the x-ray tube. The x-ray tube converts electrical energy provided by the generator into an x-ray beam. Within the x-ray tube, electrons are produced by a heated filament and accelerated toward a positively charged tungsten anode. Patient tables for fluoroscopic systems must provide adequate strength to support large patients and, at the same time, result in minimal x-ray attenuation. Anti-scatter grids are used to improve image

contrast by reducing the scattered x-rays that reach the image receptor. However, use of grids requires an increase in radiation exposure. The image intensifier converts incident x rays into a minified visible light image and, in the process, amplifies the image brightness by about 10,000 times for better visibility to the viewer. The major components of an image intensifier include an input layer to convert x-rays to electrons, electron lenses to focus the electrons, an anode to accelerate them, and an output layer to convert them into a visible image. The optical coupling system distributes light from the image intensifier output window to a video camera and other image recording devices (Fig 33).



**Figure 33: Optical coupling system**

The optical distributor may include a partially silvered, beam-splitting mirror, which directs a portion of the light from the image intensifier output window to an accessory device for image recording and passes the remainder to the video camera. A circular aperture is also included to set the proper light level required by the video camera. The aperture setting affects the appearance of noise in the fluoroscopic image. That being so, even though quite different in physical appearance and image capturing method, as resembled at the beginning of chapter 5, we can assume that a fluoroscopy system, can be

described by the defined camera model used in the project, using the vision theory previously described. In this regard, we can notice that a C-arm fluoroscopy system lends itself to a stereovision setup due its large range of possible movements, which allow acquiring images of the scene by different points of view. Longitudinal (A), vertical (B), wigwag or side-to-side (C), rotational (D), and angular movement (E) is possible by the arc housing the X-ray Tank (XRT) on the one end and the Image Intensifier (II) on the other. This architecture is designed to allow the technician to X-ray the zone of interest from different angles.

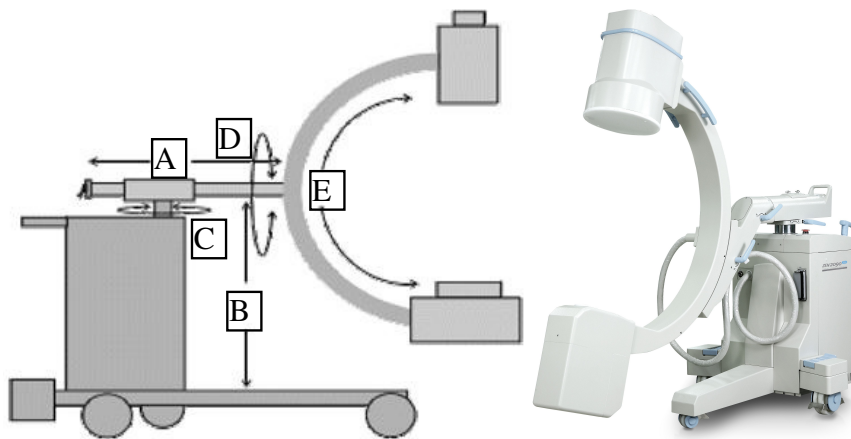


**Figure 34: C-arm fluoroscopy system setup**

## **4.2 Stereo Fluoroscopy**

A C-arm fluoroscopy system generates a bi-dimensional image, which does not provide information about the depth of the scene. A 3D fluoroscopy vision can be achieved applying the computer vision theory, described in chapter 4, to a pair of images taken by the C-arm fluoroscopy system placed in two different configurations. If the target point placed in the patient's body and the needle are visible in both images a 3D reconstruction of the scene can be performed and used to guide a biopsy procedure. One of the goals of this project is



implementing a stereovision system setup using a standard C-arm fluoroscopy system.

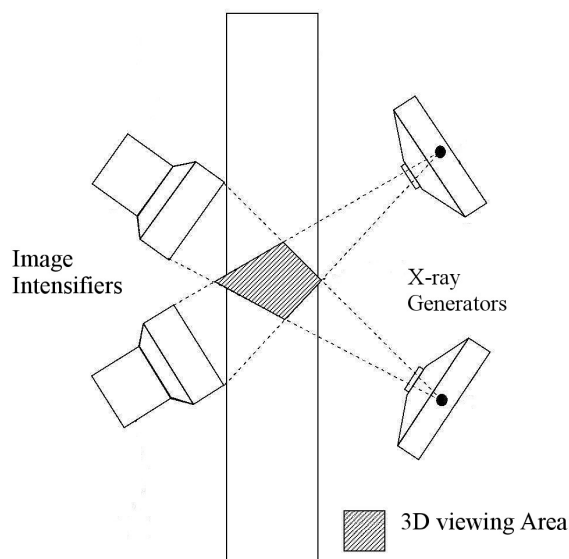


**Figure 35: stereovision fluoroscopy**

According to the computer vision theory described in chapter 3, to determine the 3D coordinates of a point knowing his two 2D coordinates in a stereo images pair, intrinsic and extrinsic parameters (described in section 3.6) of the system must be known, therefore a calibration of the system is required. Usually, for standard stereovision systems, both cameras are fixed with respect to each other, thus, extrinsic parameters do not change and they can be calculating just once. In this case, a standard calibration procedure can be applied as follow: first, each single camera is calibrated separately by taking a series of images of a calibration object whose shape is known. Thus, a stereo calibration can be performed in order to evaluate the extrinsic parameters, which denote the rotation and translation relating the camera left coordinate system to the camera right coordinate system.

For our application, the two cameras are replaced by a single C-arm

fluoroscopy system. To implement stereovision fluoroscopy, a stereo image pair from the C-arm is required, as well as a calibration of the system.

As for intrinsic calibration, it can be performed with the standard procedure, described above, while extrinsic parameters depend on the actual configuration of the C-arm taking the stereo pair. Therefore, the rotation and translation relating the C-arm coordinate system, for instance placed in position 1, to C-arm coordinate system placed in position 2, must be known for each stereo pair. However, standard C-arms fluoroscopy systems are not equipped with sensors able to provide the transformation matrix, which denote the coordinate system transformations from 3D world coordinates to 3D C-arm coordinates, or equivalently, which define the position of the optical center relative to the fluoroscopy system for each stereo pair. To overcome the problem, the solution proposed in this project is using an external measuring system able to localize the spatial C-arm's position and a proper calibration, which allows relating this localizer to intrinsic parameters of the C-arm fluoroscopy system. Several solutions can be adopted to measure spatial the C-arm's position with respect to a fix reference frame. In this project, we decide to choose an optical localizer for the following reasons:

- low cost
- easy to assembly and program
- easy to source in surgery rooms
- well suited for object's tracking and shape's recovery

### **4.3 System Overview and Working Principle**

The system designed consists of four main components: the imaging system, the optical localizer including its markers, the robotic needle-positioning system and the software. Two main processes can be distinguished in the implementation of the system: calibration and targeting.

The C-arm is provided by optical markers, which allow tracking its position with respect to the optical localizer. During the calibration process, a series of images of the calibration object is acquired by rotating the C-arm fluoroscopy along his range of motion, registering at the same time the correspondent  $i^{\text{th}}$  3D-position of the marker linked to the C-arm by the optical localizer.

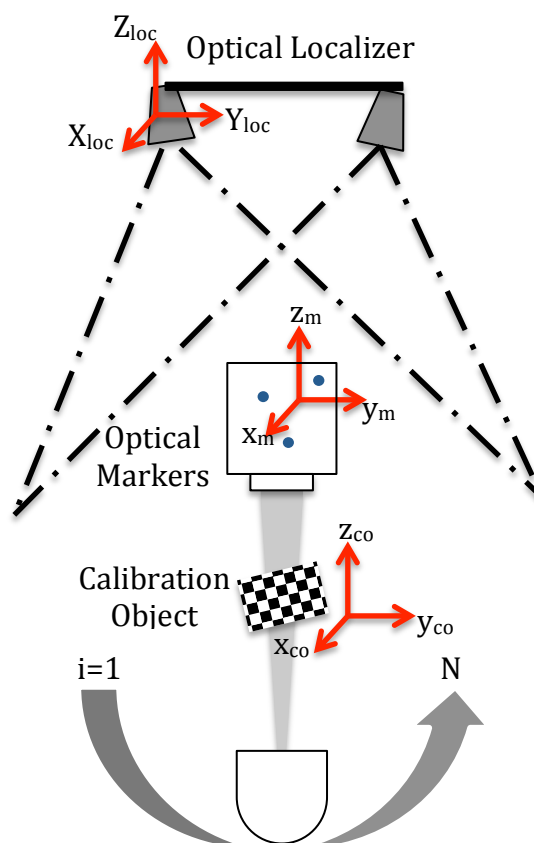


**Figure 36: C-arm Fluoroscopy system calibration**

The setup of this process is shown diagrammatically in Figure 36.

The stereo fluoroscopy calibration procedure is performed as follow: first, the position and rotation of calibration object  $^{loc}T_{co}$  is computed with respect to the optical localizer, which is kept always fixed. Thus, once the intrinsic calibration is performed by using the model described in the next paragraph, the  $i^{\text{th}}$  position and orientation of calibration object with respect to the C-arm

fluoroscopy system is calculated, or rather the rotation and the translation of the reference  ${}^{cf}T_{co}$ . Also the correspondent  $i^{\text{th}}$  rotation and the translation of the reference frame  ${}^{loc}T_m$ , associated to the marker placed on the C-arm with respect to the optical localizer is computed. Hence, using a sequence of homogeneous transformation matrices, we are able to calculate, for each  $i^{\text{th}}$  image recorded, the position of the optical center of fluoroscope, indicated as  ${}^mT_{Cf}$  with respect to the optical marker as follow:

$${}^mT_{Cf} = inv[{}^{loc}T_m] \cdot {}^{loc}T_{co} \cdot inv[{}^{cf}T_{co}] \quad \forall i = \{1..N\} \quad [56]$$

which yields to a vector of N homogenous matrices.

$${}^mT_{Cf} = \begin{bmatrix} {}^mR_{Cf} & {}^mP_{Cf} \\ 0 & 0 & 0 & 1 \end{bmatrix} \quad [57]$$

To evaluate the calibration error on the position and rotation, we can compute the average value for both position and rotation. The average value for the position can be easily computed, averaging the 3D coordinates (x,y,z) of the N vector  ${}^mP_{Cf}$ . As for the rotation between the marker and the optical center of fluoroscope, calculating an average value for N rotations matrices  ${}^mR_{Cf}$  is slightly more complex.

The Euclidean formulation of the rotation average is based on the Euclidean metric for rotation matrices, stated as:

$$d_f(R_1R_2) = \|R_1 - R_2\|_F \quad [58]$$

Equation 58 is the Frobenius norm of the difference between two rotation matrices and the same norm is noted to be bi-invariant. Based on this norm, the authors of [33] defines the average rotation matrix of a sequence of N rotations  $R_i$  as the solution of the following minimization problem:

$$\bar{R}_F = \arg \min_R \sum_{i=1}^N \|R_1 - R_2\|_F^2 \quad [59]$$

Since a rotation matrix may be represented via any of the existing rotational representations such as quaternions or rotation vectors, an approximate solution of [59] can be the average quaternion solution for a sequence of N quaternions  $q_i$  as:

$$\bar{q} = \sum_{i=1}^N q_i / \left\| \sum_{i=1}^N q_i \right\| \quad [60]$$

The above average is not based on a bi-invariant norm, but as shown in [34] is an approximate solution of the analogous optimization problem:

$$\bar{q} = \arg \min_R \sum_{i=1}^N \phi^2(q^* q_i) \quad [61]$$

where the  $*$  notation denotes conjugate quaternion and the operation between  $q^*$  and  $q_i$  is standard quaternion multiplication. It is also demonstrated in [34] that the quaternion-based solution does not give identical results to the Euclidean rotation matrix solution, and in fact, it provides a more accurate approximation of the Riemannian average.

Once the calibration is completed, the software allows the user to update in real time the extrinsic parameters of the C-arm fluoroscopy system taking the stereo image pair. During the targeting process, a stereo image pair of the target and of the robotic end-effector bearing the needle is acquired. Utilizing the user interface and targeting software the relative orientation of the needle to that of the target can be compute, as well as the distance from the entry point to the target. The translational and rotational needle adjustment for accurate targeting is determined in the robot space coordinates allowing to set the proper joint's configuration, finally the surgeon can insert the needle until the computed depth is reached. This setup is shown diagrammatically in Fig. 37.

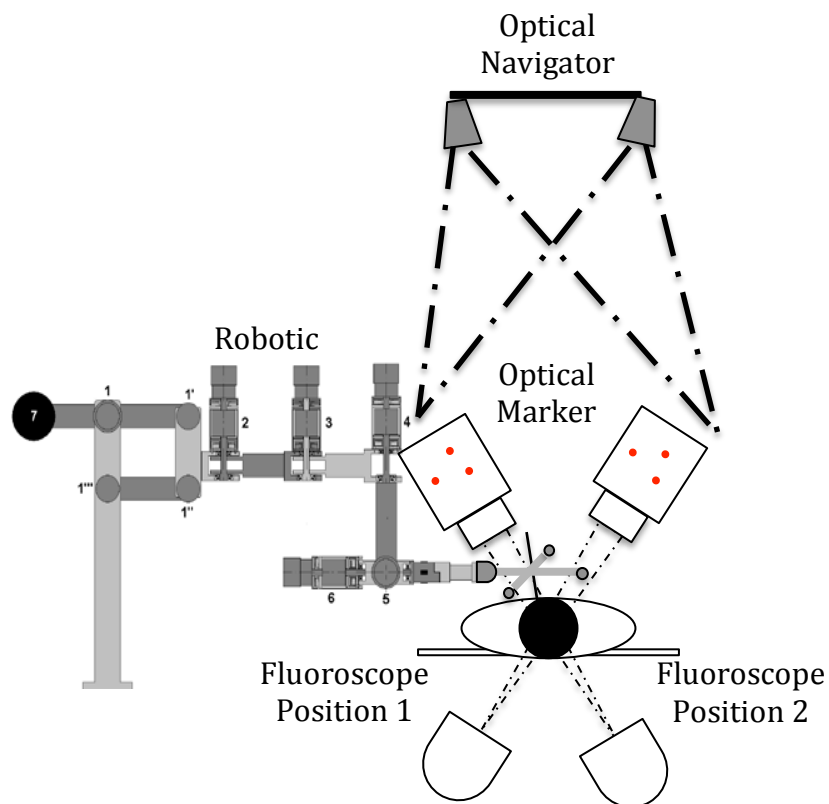


Figure 37: Biopsy procedure fluoroscopy based setup

## 4.4 Camera Calibration

For this project, a homemade stereovision system was built. The system, as well the camera used to simulate the C-arm fluoroscopy system, both described in detail in Chapter 6, were calibrated using an advanced geometric camera calibration technique, tested in cooperation with Computer Integrated Manufactory Laboratory (CIMLab) at University of Toronto. This technique employs a sophisticated lens distortion model that takes the radial, tangential, and prism distortion into account, and achieves a precise localization of the control points with a novel refinement process using a frontal image concept and an advanced digital image correlation (DIC) scheme [35].

For the ideal pinhole model, assuming that the world coordinate is placed on

the calibration target with its surface as the  $XY$  plane, the relation between the three-dimensional world coordinate of a calibration target point  $\mathbf{M} = [X_w, Y_w, Z_w]^T$  and its corresponding location  $\mathbf{m} = [u, v]^T$  in the image plane can be expressed as:

$$s \begin{Bmatrix} m \\ 1 \end{Bmatrix} = A[R \ T] \begin{Bmatrix} m \\ 1 \end{Bmatrix}, A = \begin{bmatrix} \alpha & \gamma & u_o \\ 0 & \beta & v_o \\ 0 & 0 & 1 \end{bmatrix} \quad [62]$$

where  $s$  is a scale factor;  $A$  is the intrinsic matrix, with  $\alpha$  and  $\beta$  the horizontal and vertical focal length in pixel unit,  $\gamma$  the skew factor, and  $(u_o, v_o)$  the coordinates of the principal point;  $R$  and  $T$  are the extrinsic parameters that denote the rotation and translation relating the world coordinate system to the camera coordinate system. Due to nonlinear optical distortion, equation 62 is not sufficient for accurate camera calibration. In spite of the fact that some very complex models exist, in practice they induce more instability rather than accuracy because of the high order distortion components. Here, the lens distortion is compensated by:

$$u' = (1+a_0r^2 + a_1r^4 + a_2r^6)u + s_0r^2 + (p_0 + p_2r^2)(r^2 + 2u^2), \quad [63]$$

$$v' = (1+a_0r^2 + a_1r^4 + a_2r^6)v + s_1r^2 + (p_1 + p_3r^2)(r^2 + 2v^2), \quad [64]$$

$$r^2 = u^2 + v^2, \quad [65]$$

where  $(a_0, a_1, a_2)$ ,  $(s_0, s_1)$ , and  $(p_0, p_1)$  represent the radial, prism, and tangential distortion coefficients, respectively,  $(u, v)$  denotes the distortion-free pixel location, and  $(u', v')$  is the corresponding distorted point.

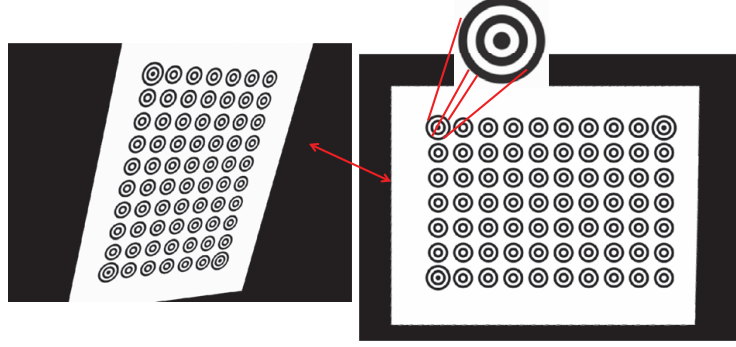


**Figure 38: Calibration ring template**

The correlation coefficient function is:

$$C = \sum_{i=1}^N [af(x_i y_i) + b - g(x'_i y'_i)]^2 \quad [66]$$

where  $a$  is a scale factor,  $b$  is an intensity offset, and  $f(x_i, y_i)$  and  $g(x'_i, y'_i)$  denote the intensity values at the  $i$ -th pixel in the template and frontal images, respectively. The template pattern is a square sub-image of  $N$  pixels with its center as the center of the circular target point. Denoting the sub-image center as  $(x_0, y_0)$  and its shift amount between two sub-images as  $(u, v)$ , the correlation shape function considering both translation and rotation is:

$$x'_i = x_i + u + u_x(x_i - x_0) + u_y(y_i - y_0) \quad [67]$$

$$y'_i = y_i + v + v_x(x_i - x_0) + v_y(y_i - y_0) \quad [68]$$

where  $u_x, u_y, v_x,$  and  $v_y$  are coefficients of the shape function. To determine the eight unknowns  $(u, v, u_x, u_y, v_x, v_y, a, b)$ , the Newton–Raphson algorithm is employed to minimize  $C$  in Eq. (66). With the detected  $(u, v)$ , the location of each control point in the frontal image can be directly determined. Then, these points in the frontal image are reversely projected back to the image plane to achieve hyper-accurate localization of the control points.

The rationale of the proposed method is that although the imprecise control points detected in the raw images lead to inaccurate camera calibration



parameters, they offer good initial information about the relation between the camera and each scene, which can be further processed to achieve very accurate localization of the control points. This information helps detect the camera intrinsic and extrinsic parameters as well as the world coordinates of the control points with high accuracies.

It is important to notice that, for a future application in a real surgery room, such distortion model is well suited to describe the behavior of an actual fluoroscope, however in this case a 3D calibration object should be used to replace the board bearing the image pattern and the software for feature extraction should be accordingly adjusted. For our stereo system setup, the residual of the calibration, named re-projection error and defined, as the root-mean-square-error (RMSE) between the projection of the control points to the image planes and their measured locations, was 0.002 pixels.

## **4.5 Optical Navigator User Interface and Software**

An essential part of the stereovision system is the software, which allows the user to visualize the optical markers, on a graphic interface (Fig. 39), reconstructing their 3D shape and measuring their position with respect to the cameras coordinate system.

In particular, the graphic user interface implemented in Matlab and shown below is able to:

- Acquire in real time images from the cameras
- Remove the noise, filter and calculate the 2D coordinates of each visible centroid of the marker
- Based on the calibration data, calculate the correspondences between the 2D coordinates in each view
- Triangulate 2D coordinates of the correspondent points of the stereo pair and calculate the 3D position of the marker's center of mass with

respect to the cameras.

- Associate a coordinates system to each visible 3D object and plot it on a dedicated window.

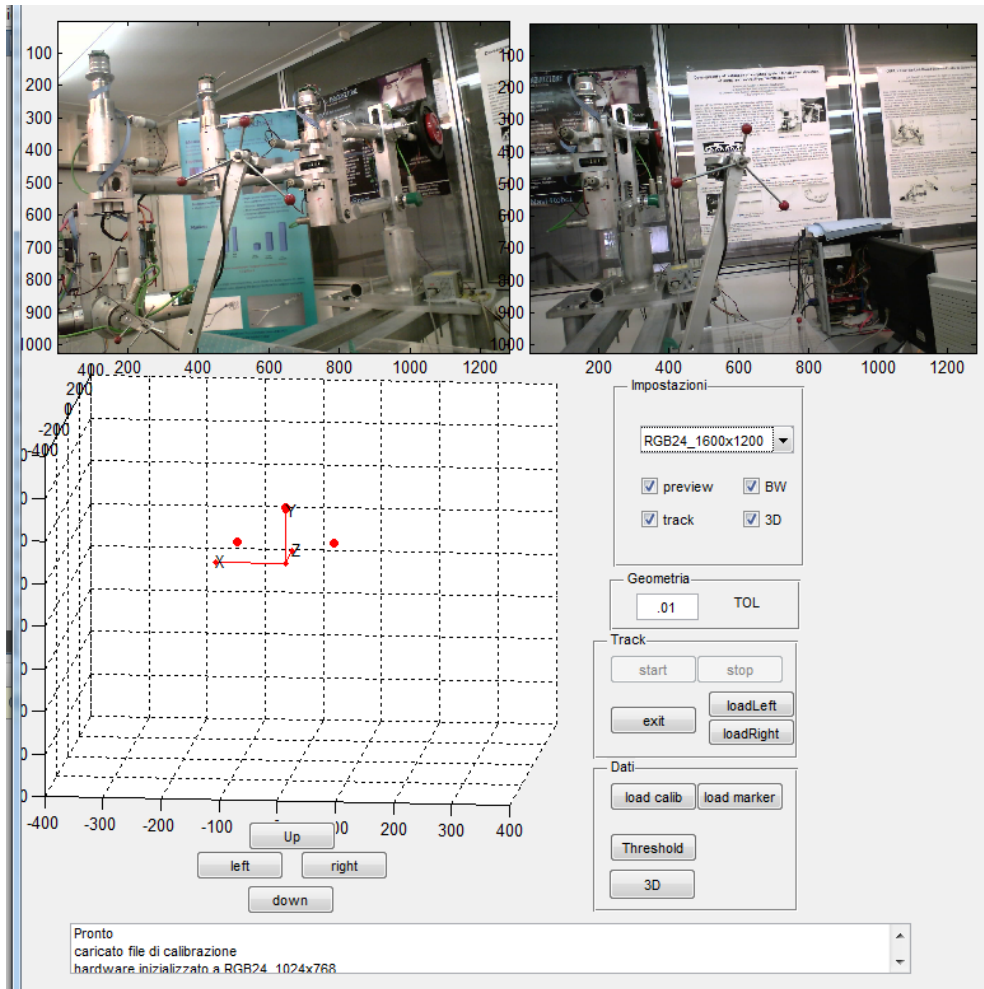
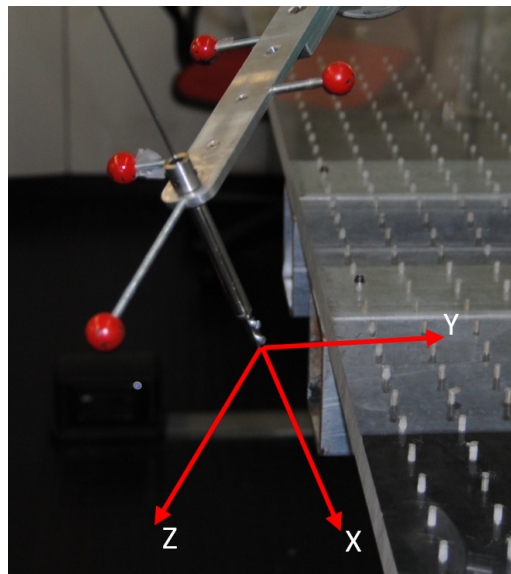


Figure 39: Optical navigator user interface

## 4.6 End-effector and Needle Orientation Determination

We define the needle coordinate system (NCS) with respect to the robot reference frame as follow: the z-axis is located on the axis of symmetry of the end-effector frame, the x-axis is orthogonal to the plane of the frame and

aligned to the alignment cylinder, and y-axis is calculated by the right-hand rule. Finally, the origin of the system is located on the tip of the needle. The needle axis is down along the x-axis and needle position coincides with the origin of the coordinate system. If the subscript denotes the object of interest and the superscript denotes the reference coordinate system, the needle position and orientation can be defined by a homogenous transformation matrix  ${}^{RCS}R_{init\_needle}$ .



**Figure 40: Needle system coordinates**

The four spherical markers placed on the robot's end-effector described in section 2.3 and visible in the figure above, allow defining a second coordinate system with respect to the marker seen by the C-arm fluoroscopy system and represented by the homogenous transformation matrix  ${}^M R_{init\_needle}$

The origin of the coordinate system coincide with the center of mass the markers (point B in fig. 41). The direction of the x-axis is the normal to the plane that best fits the 3D coordinates of the spherical markers via a least squares regression. The z-axis direction is parallel to the axis of symmetry of the end-effector's frame and passes through the origin; finally, the y-axis is

calculated by the right hand rule.

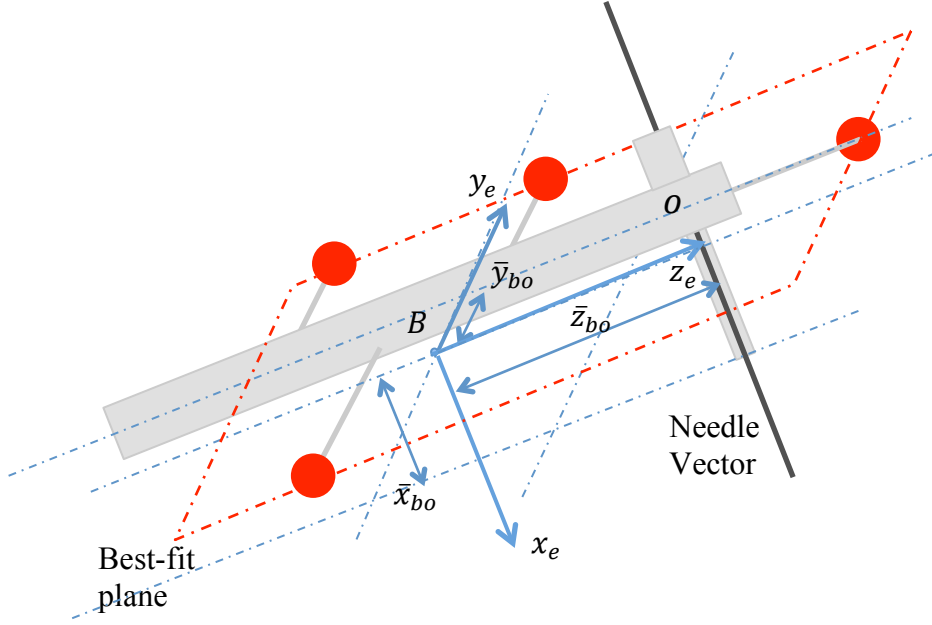


**Figure 41: Needle system coordinate reconstructed**

The offset between the origin of  ${}^M R_{init\_needle}$  and the origin of  ${}^{RCS} R_{init\_needle}$  was determined by touch probe measurement on the CMM to be -82.52 mm on the x-direction ( $x\_off$ ), -11,58 on the y-direction ( $y\_off$ ) and -38.32 on the z-direction ( $z\_off$ ).

Hence, via a fixed translation  ${}^{C-arm} R_M = \begin{bmatrix} 1 & 0 & 0 & x\_off \\ 0 & 1 & 0 & y\_off \\ 0 & 0 & 1 & z\_off \\ 0 & 0 & 0 & 1 \end{bmatrix}$  we can

calculate the transformation matrix:

$${}^{C-arm} R_{init\_needle} = {}^{C-arm} R_M \times {}^M R_{init\_needle} \quad [69]$$

Thus, knowing the 3D coordinates of the target and of the entry point reconstructed in the C-arm space respectively,  ${}^{C-arm} P_T$   ${}^{C-arm} P_E$  we can map these points into to the needle coordinates system as follow:

$${}^{init\_needle}P_T = {}^{C-arm}R_{init\_needle}^{-1} \times {}^{C-arm}P_T \quad [70]$$

$${}^{init\_needle}P_E = {}^{C-arm}R_{init\_needle}^{-1} \times {}^{C-arm}P_E \quad [71]$$

that allows mapping the target point and entry point into the robot coordinate system as follow:

$${}^{RCS}P_T = {}^{RCS}R_{init\_needle} \times {}^{init\_needle}P_T \quad [72]$$

$${}^{RCS}P_E = {}^{RCS}R_{init\_needle} \times {}^{init\_needle}P_E \quad [73]$$

## 4.7 Targeting Computation

This paragraph describes the mathematical computations implemented in determining the required needle translation and rotation for targeting.

The targeting process starts selecting the target point and the needle entry point in both images of the stereo pair. Thus, these points and the 2D coordinates of the marker denoting the needle position are triangulated and reconstructed with respect to the C-arm fluoroscopy reference frame. The 3D coordinates (x, y, z) of the target, the needle entry point are mapped in the robot reference frame using respectively the equations 72 and 73.

The entry point coordinate (yellow marker) and target coordinate (green marker) can be used to provide a new vector  $\overrightarrow{ET}$ , to which the needle is adjusted. Hence, the procedure attempts to place the tip of the needle, from the initial position, at the entry point, aligning the needle vector to  $\overrightarrow{ET}$  vector. The distance between the access point (yellow marker) and the target (depth penetration) is also calculated and displayed on the user interface.

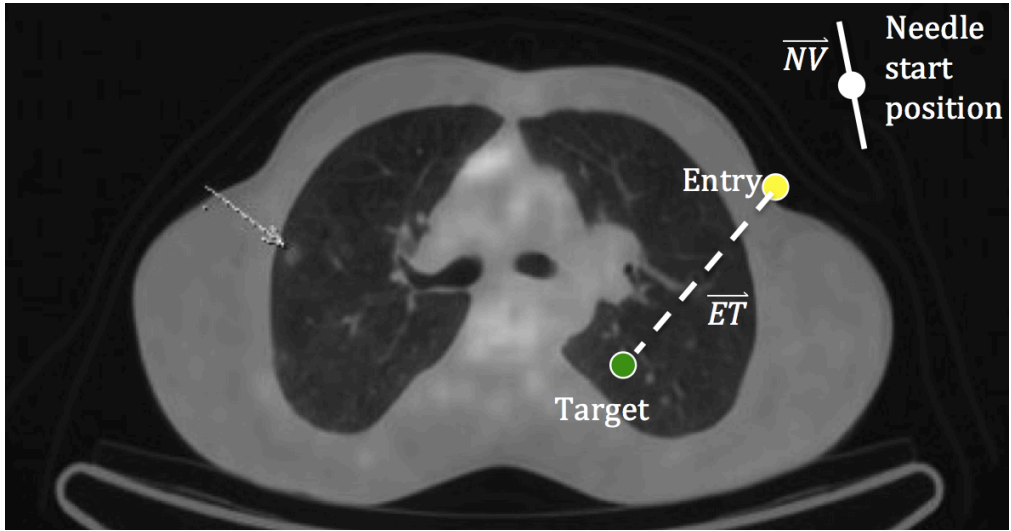


Figure 42: Needle path planning

The required translation to place the tip of the needle at the entry point location can be computed simply as:

$$(x, y, z)_{adj} = (x, y, z)_{entry} - (x, y, z)_{init} \quad [74]$$

The computation of the necessary needle orientation adjustment is similar to that of the translation computation. Given the initial needle vector  $\vec{NV}$ , and the final vector  $\vec{ET}$ , the angles  $\varphi$  and  $\theta$  with respect to the XZ and YZ-planes are computed as:

$$\theta_{adj} = \theta_{target} - \theta_{init} \quad [75]$$

$$\varphi_{adj} = \varphi_{target} - \varphi_{init} \quad [76]$$

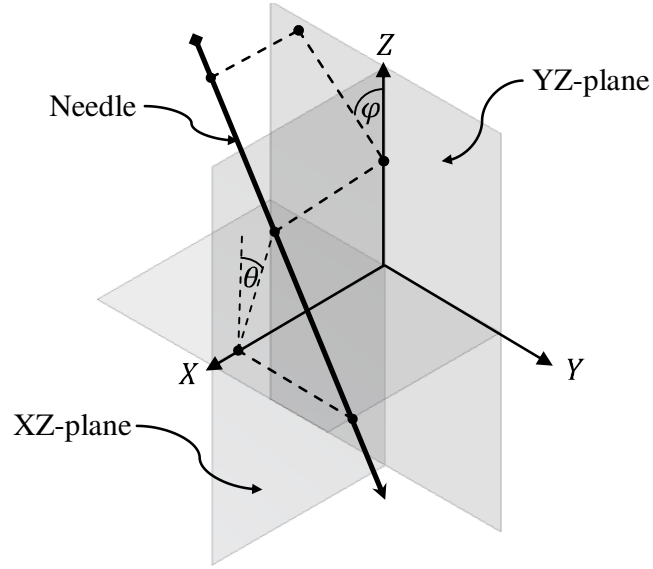


Figure 43: Rotation angles and planes

The desired orientation can be now evaluated as follow:

$${}^{RCS}R_{adj\_needle} = {}^{RCS}R_{init\_needle} \cdot R_x(\varphi) \cdot R_y(\theta) \quad [77]$$

where  $R_x(\varphi)$  and  $R_y(\theta)$  are two homogenous matrices denoting two rotations respectively, around the NCS x-axis and the NCS y-axis of angles respectively  $\varphi$  and  $\theta$ .

Once translation and rotation have been computed, the next step is required coordinates system transformation, which can be written as follow:

$${}^{adj\_needle}R_{init\_needle} = [{}^{RCS}R_{adj\_needle}]^{-1} \times {}^{RCS}R_{init\_needle} \quad [78]$$

Given the matrix  ${}^{adj\_needle}R_{init\_needle}$  describing the final position and orientation in the RCS and the location of the entry point and target point in the robot coordinates system  ${}^{RCS}P_E, {}^{RCS}P_T$  the vector  $q = [q_1, q_2, q_3, q_4, q_5, q_6]^T$  containing the six joint's variables can be computed by inverting the robot

kinematic. Since the inverse kinematic of the robot does not take into account the geometric error, the vector  $q$  must be corrected using the direct kinematic that instead, contains the error parameters for geometric errors compensation. To do so, the vector  $q$  is used to evaluate the position of the tip needle located at the entry point  ${}^{RCS}P_{E\_corr}$  and at the target point  ${}^{RCS}P_{T\_corr}$  via direct kinematic, thus minimizing the error:

$$Err = \sqrt{({}^{RCS}P_{E\_corr} - {}^{RCS}P_E)^2 + ({}^{RCS}P_{T\_corr} - {}^{RCS}P_T)^2} \quad [79]$$

the vector  $q^* = [q_1^*, q_2^*, q_3^*, q_4^*, q_5^*, q_6^*]^T$  of the joint's angles that take into account the geometric errors can be computed.

## 4.1 GUI Design and Operation

The control center of the described positioning system is the surgeon operated user interface. This interface aids the surgeon in defining the relative needle and target and entry positions by requesting specific actions from the operator. With successful points selection the algorithms described in previous section are implemented. The command screen, shown in Fig. 44, has three sub-frames called respectively: 2D Space, 3D space and Command and allows the definition of all points required for targeting.

The 2D space sub frame allows to take/import and display the two targeting images taken at each respective position of the image acquisition system, to record the correspondent position of the optical marker for each image position by using the optical localizer and finally to run the calibration for the current image stereo pair. The sub-frame called Command is the selection point's frame, provided by selection buttons for the target, and entry points as well as the triangulation, clear and save buttons respectively to calculate the 3D position of all the points of interest, clear wrong/old selected points and store the 3D coordinates of the points used for targeting.



Finally, in the 3D space sub frame, the NCS (blu) is plotted as well as: the target point, the ET vector and start needle position. This sub frame also allows measuring and display distances and angles between points or lines selected, orientate the 3D plot for better displaying and align the needle for insertion by means of the align button.

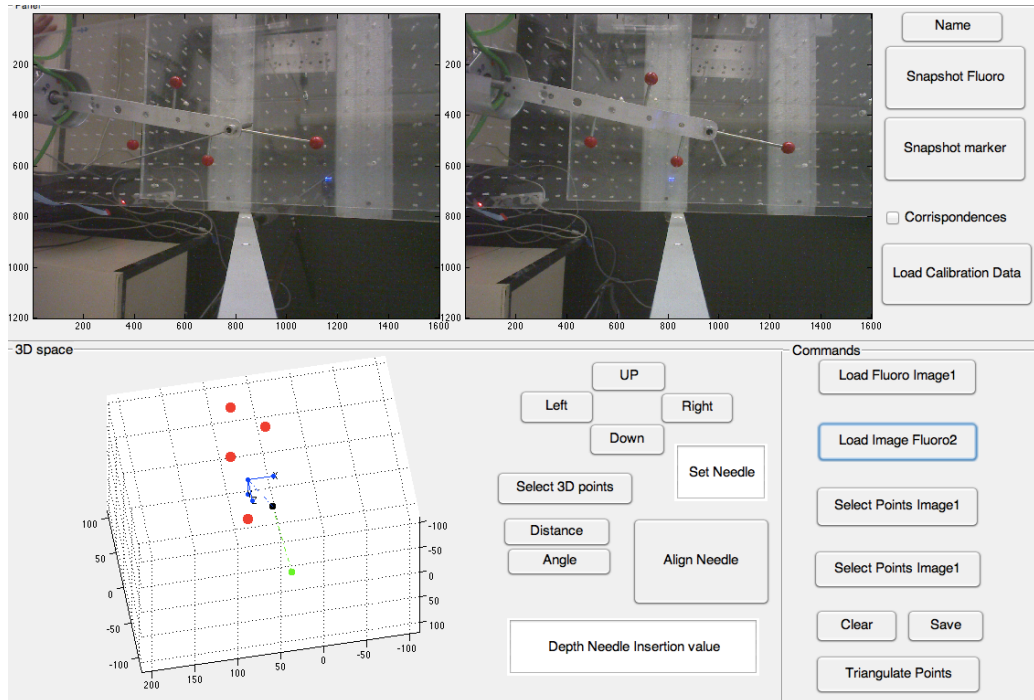


Figure 44: C-arm fluoroscopy system user interface

## 5. CT Based Biopsy

This chapter gives an overview of the components of the system, as well the working principle, which allows integrating the Navi-Robot with a CT scanner in order to guide a precision biopsy. Each step of the procedure implemented to achieve this goal is described as well as software and graphical user interface.

To perform needle biopsy, a registration procedure is required to map the coordinates of the target and the needle from the CT image space to the robot space. In this regard, two different strategies were tested. The first one was

performed using three spherical markers placed on the body of the patient and the end-effector of the robot as a touch probe. In the second one, the system not only comprises the robot and a CT scanner, but an optical localizer is used as supplementary element of the system. Both strategies of course require a graphical user interface, which include the visualization software for CT images and the command control center of the robot.

## 5.1 Graphical User Interface

To localize automatically the position of the spherical markers in the CT coordinates, dedicated software (Fig. 45) was implemented in matlab. The software allows reading and importing the images in DICOM format, selecting the plane in which the images are taken (sagittal, axial, coronal, etc.) and localize the position of the markers with respect to the CT coordinates system.

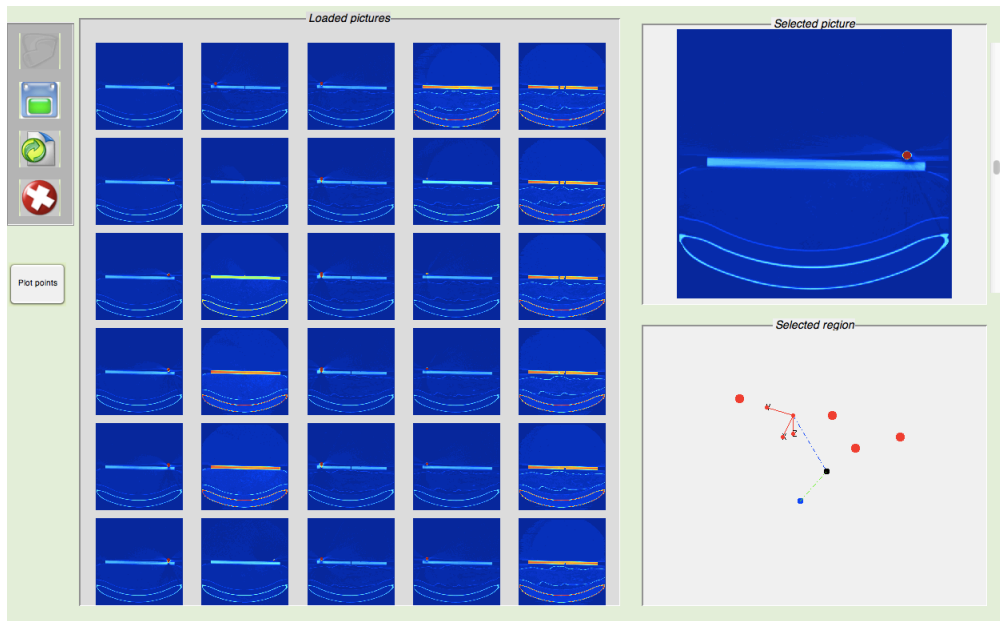


Figure 45: CT scan user interface

In order to localize the spherical marker, each slice first is filtered and segmented. To find the center of mass of the marker, the algorithm implemented searches for the centroid of circular pixel region of the central

section. This section can be determined by searching for the pixel region whose diameter is equal to that of the actual sphere scaled by a known factor. Since the maximum section could not coincide with none of the slice acquired due to the fixed step of acquisition, an interpolation is required. Thus, for each slice, the 2D coordinates of the centroid belonging to the section of the sphere visible in the current slice are stored. Finally, all the 2D coordinates belonging to the same marker, are interpolated and knowing the distance between each slice, the 3D position of the center of mass of the marker is calculated. The software was implemented inside a graphical user interface, which also allows the user to select the entry point and the target point in the CT volume, displaying the points on a 3D plot. The interface also allows plotting in a dedicated window, the needle entry point, the target point and the coordinate system associated to the needle that is hold by end-effector of the robot.

## **5.2 Procedure Workflow for Registration Strategy I**

The first registration strategy tested was implemented using the robot in passive mode as touch probe to localize the marker with respect its coordinates system.

The workflow for the robotically assisted procedures is the following:

1. The patient is positioned on the table; three spherical markers are placed on his body. In order to minimize the marker displacement due to the motion of the patient two of them are placed on the clavicles and one on the pelvis, or rather on parts of the body that are less subject to movements.
2. A series of CT scans are obtained
3. The scans are transferred from the operator's workstation to the CT workstation using the DICOM protocol
4. The user interface software allows the physician to select the plane of scan of interest and the region to be biopsied (entry location and target point)
5. The robot in passive mode is guided to touch the markers to achieve the

registration

6. The software calculates the correct needle depth insertion which is marked on the needle
7. The robot automatically orients the end-effector carrying the needle-guide and places it to at the correct entry point.
8. The biopsy sample is taken by inserting the needle through the needle-guide

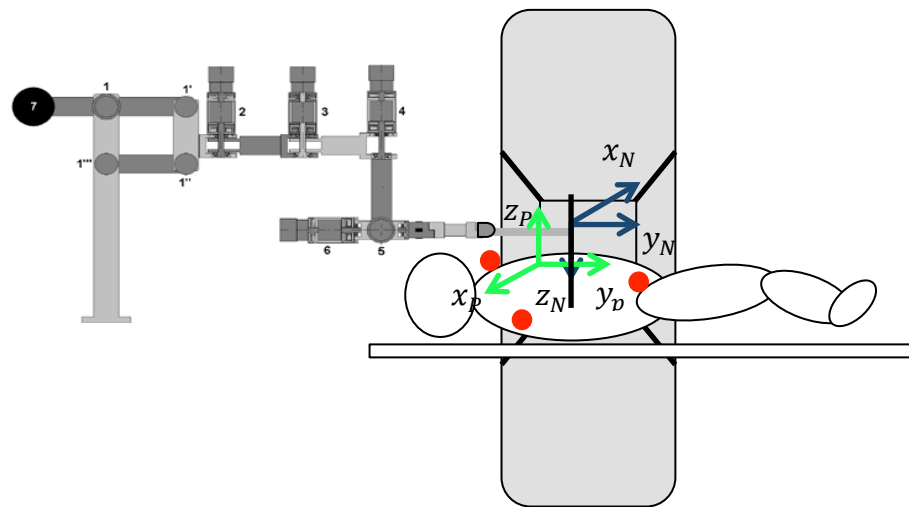


**Figure 46: Biopsy procedure CT based setup**

Since the target point and entry point are visible in the CT images as well as the markers on the patient, their coordinates can be expressed in the coordinates system of the robot.

### **5.3 Procedure Workflow for Registration strategy II**

Although the first registration strategy has shown good result in the laboratory testing using a rigid body in place of the patient, an issue related to this method is the possible displacement of the markers not only caused by little movement of the patient but even by the touch of the end-effector attempting to register the robot position. Therefore, a second approach was proposed to avoid the

problem, which, however, requires a further component and thus a major cost. In the second strategy, hence the system comprises even the optical localizer including the relative software already developed. The end-effector of the robot moreover must be provided by optical markers to perform the registration. The workflow of the robotically assisted procedure is the following:

1. The patient is positioned on the table and three spherical markers are placed on his body in the same way as previously defined.
2. A series of CT scans are obtained
3. The scans are transferred from the operator's workstation to the CT workstation using the DICOM protocol
4. The user interface software allows the physician to select the plane of scan of interest and the region to be biopsied (entry location and target point)
5. The robot end-effector in passive mode is guided in the operatory scene, with both end-effector markers and patient markers visible by the optical navigator to perform the registration
6. The software calculates the correct needle depth insertion which is marked on the needle
7. The robot automatically orients the end-effector carrying the needle and places it to at the correct entry point.
8. The biopsy sample is taken by inserting the needle through the needle guide

In this case the registration involves the use of the optical localizer, thus there is no need to touch the markers on the body of patient, risking causing displacement and thus adding inaccuracies into the system. The coordinate systems we use are shown in Fig. 47 and defined as follows:

- (1) Localizer coordinate system Loc\_CS, defined during the calibration procedure described in paragraph 4.4
- (2) Needle coordinate system, Needle\_CS. This coordinate system is defined in the same manner as explained in paragraph 4.7 thus, denotes the orientation and the position of the needle with respect to the robot reference frame (RCS).
- (3) The patient's body coordinate system Patient\_CS, defined with respect to

the markers placed on patient. The coordinates of the spherical markers are expressed in the CT image space and their computation will be shown in the next section. The origin of the coordinate system is placed in the center of mass of the markers, the z-axis is orthogonal to the plane that best fits the 3D coordinates of the spherical markers via a least squares regression. The y-axis is along the direction between the origin of the system and marker placed on the pelvis; the x-axis is defined by the right-hand rule.

All of these coordinate systems are used to map the target and the needle entry point from the CT image space to the robot coordinate system.

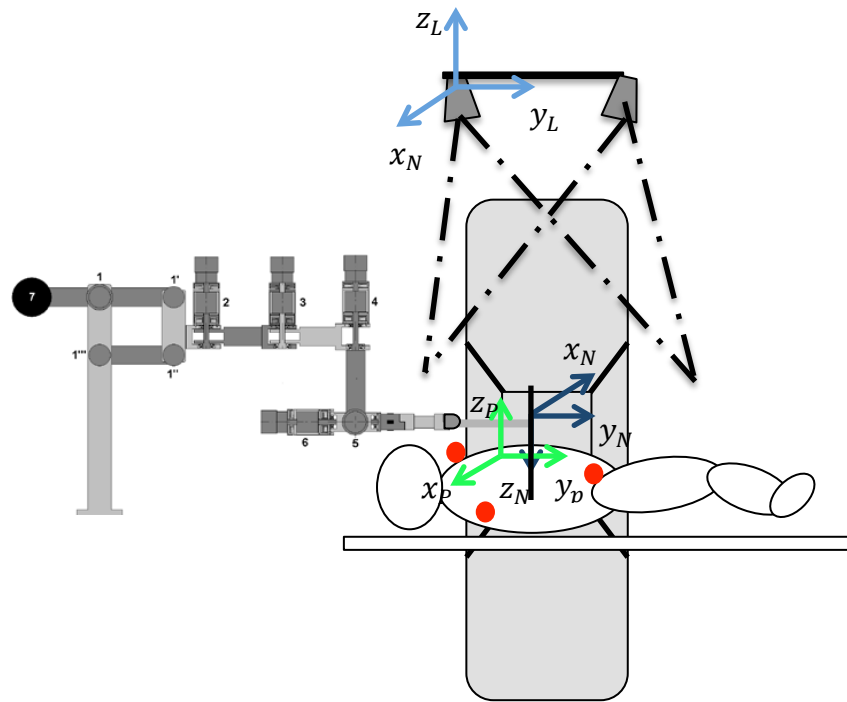


**Figure 47: Biopsy procedure CT based setup using registration strategy II**

## 5.4 Targeting and Coordinate System Transformation

For both strategies, the targeting computation is identical to the process described in paragraph 4.6. As for strategies I, the robot registration is achieved automatically by using the robot as navigator, touching the spherical markers with its own end-effector bearing the needle.

As for the second registration strategy, a further coordinate transformation is required. The process can be described as follow:

Step 1: Query the localizer to read the orientation of the spherical markers place on the end-effector of the robot. This orientation is given with respect to the optical localizer coordinate system. As result, we obtain  ${}^{Loc\_CS}R_M$ .

Step 2: Query the localizer to read the position of the spherical markers place on the patient, denoting the Patient\_CS. This orientation is given with respect to the optical localizer coordinate system. As result, we obtain  ${}^{Loc\_CS}R_{Pat\_CS}$ .

Step 3: given the 3D coordinates of the target and of the entry points reconstructed in the CT image space respectively,  ${}^{CT}P_T$   ${}^{CT}P_E$  the coordinates of these point with respect the patient coordinates system can be calculated as:

$${}^{Pat\_CS}P_T = {}^{Loc\_CS}R_{Pat\_CS}^{-1} \times {}^{CT}P_T \quad [80]$$

$${}^{Pat\_CS}P_E = {}^{Loc\_CS}R_{Pat\_CS}^{-1} \times {}^{CT}P_E \quad [81]$$

Step 4: compute the transformation matrix to map the orientation of the needle with respect to the localizer coordinates system, given the fix transformation  ${}^M R_{init\_needle}$  described in section 4.6

$${}^{Loc\_CS}R_{init\_needle} = {}^{Loc\_CS}R_M \times {}^M R_{init\_needle} \quad [82]$$

Step 5: Given the orientation of the needle in the robot coordinates

system  ${}^{RCS}R_{init\_needle}$ , compute the transformation matrix to map the patient coordinate system to the robot coordinates system:

$${}^{RCS}R_{Pat\_CS} = {}^{RCS}R_{init\_needle} \times {}^{Loc\_CS}R_{init\_needle}^{-1} \times {}^{Loc\_CS}R_{Pat\_CS} \quad [83]$$

Step 6: map the coordinates of needle entry point and target point with respect to the robot coordinates system

$${}^{RCS}P_T = {}^{RCS}R_{Pat\_CS}^{-1} \times {}^{Pat\_CS}P_T \quad [84]$$

$${}^{RCS}P_E = {}^{RCS}R_{Pat\_CS}^{-1} \times {}^{Pat\_CS}P_E \quad [85]$$

Step 7: since we can calculate the desired needle orientation  ${}^{RCS}R_{adj\_needle}$  using the targeting process described in paragraph 4.6, we can compute the transformation matrix between the actual needle orientation and the desired needle orientation as:

$${}^{adj\_needle}R_{init\_needle} = [{}^{CT}R_{adj\_needle}]^{-1} \times {}^{CT}R_{init\_needle} \quad [86]$$

which allows computing the inverse robot kinematic to evaluate the configurations of the joints to reach the desired end-effector orientation and position.

## 6. Testing and Results

This chapter describes the testing procedures and discusses the results obtained. The system was tested in the laboratory environments. The laboratory testing procedure provided quantitative results regarding calibration accuracy,



mechanical system repeatability, and targeting accuracy and system functionality.

## **6.1 Laboratory Testing**

Due to the constraints on sourcing the fluoroscopic imaging system, a simulation of the final implementation environment was necessary. A first setup was built to simulate the C-arm fluoroscopy system using a digital camera. This allowed thorough testing of the system to determine mechanical design accuracy and repeatability, as tests could be repeated in a controlled environment.

While to test the accuracy of the system composed of the Navi-Robot and of the CT scanner, a second experiment was performed using a setup comprising a rigid object provided by spherical marker and a target to simulate the body of the patient. This second setup also allowed a basis for algorithm testing during the development of the system.

## **6.2 Setup I: Calibration and Targeting**

The optical localizer was built using two cameras, Lifecam NX-6000 max resolution 2Mp, were mounted on a tripod support allowing a variable baseline within the range 200-450 mm. To measure the position of objects of interest, optical markers was built using rigid steel high accuracy drilled steel spheres, diameter 15.05 mm and red painted.

A camera simulating the fluoroscope (Philips SPC1000NC max res 1,5MP, adopted 1290x960) has been fixed to a rigid beam mounted on a configuration resembling that of the C-arm and three optical markers were rigidly attached on the by using 3 screws fixed at 120° with respect to each other.

The calibration procedure was performed as follow: a ring template was attached on a fixed Plexiglas board in the robot workspace. Thus, changing the angle of the beam in order to simulate the C-arm rotation, a series of images were recorded by the camera simulating the fluoroscope, which will be call

since now on, F-cam. For each image taken from the F-cam the position of the marker was recorded by using the optical navigator. A picture of the setup is shown below:

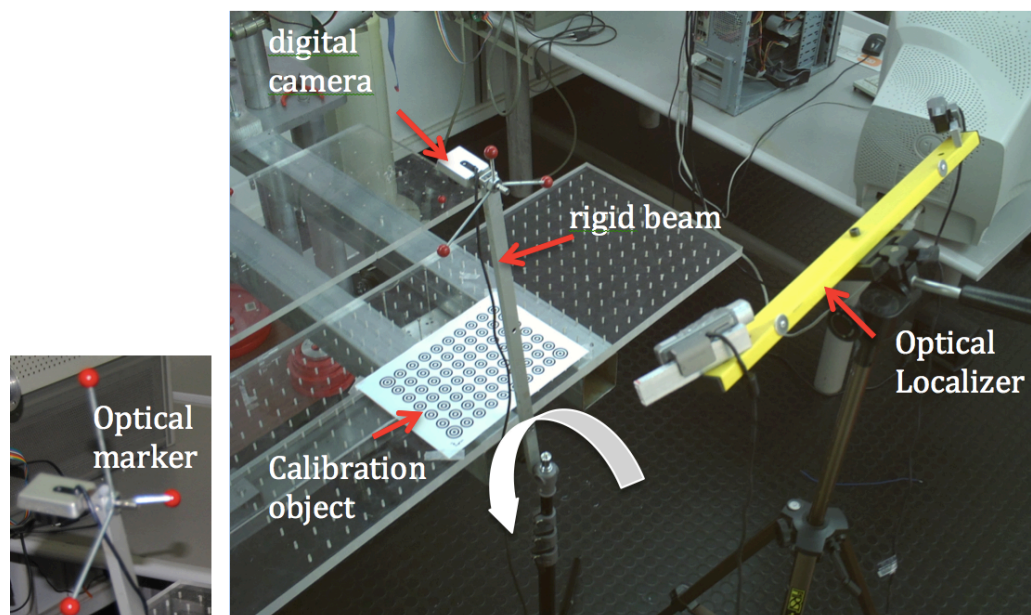


Figure 48: Optical marker (left) F-cam calibration setup (right)

Using the calibration algorithm describe in section 4.3, the position and the orientation of coordinate system related to the calibration object was calculated, knowing the position of the optical localizer with respect to the calibration object, the position and orientation of the F-cam optical center with respect to the marker linked to the F-cam was computed.

### 6.3 Optical Localizer Accuracy

The accuracy of the optical localizer, which comprises even the software used for 3D reconstruction, was estimated moving the end-effector with the spherical markers over the workspace and comparing the six known measured distances between the four marker to the six distance calculated by reconstructing and triangulating the coordinates of the markers using the

optical localizer (Fig. 49).

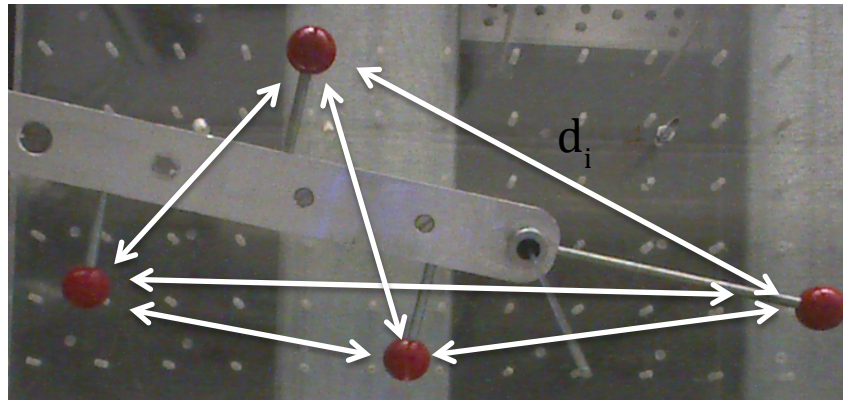


**Figure 49: known distances between marker**

The measurements were tested over the robot workspace within a volume of  $300 \times 200 \times 500 \text{ mm}^3$  collecting 40 different end-effector poses. To evaluate the total error the 6 distances were combined using the formula:

$$Err = \sqrt{\sum_{i=1}^6 (d_i^M - d_i^T)^2 / 6} \quad [64]$$

where  $d_i$  is the  $i^{\text{th}}$  inter-distance between two end-effector markers.

The statistical error between the known distances and reconstructed distances are shown in Table 3.

**Table 3: Optical localizer accuracy results**

Parameters	Error
Standard Deviation [mm]	0.7
Range [mm]	1.7
Minimum [mm]	0.5

Maximum [mm]	2.2
N° Pose [mm]	40

## 6.4 Calibration Procedure Accuracy

The average rotation matrix, describing the orientation of the optical center of the F-cam with respect the marker coordinate system linked to the F-cam, was evaluated by converting the rotation matrices in quaternions and averaging them according to the formulation described in section 4.3 For the position error, the mean, the maximum error and the standard deviation are reported in the table below:

**Table 4: Calibration accuracy result**

Coordinate	Mean [mm]	Max Error [mm]	Standard Deviation [mm]
x	0.85	1.22	0.74
y	0.92	1.43	0.82
z	0.78	1.44	0.76

Calibration accuracy as well as done for the optical navigator was estimated moving the end-effector with the spherical markers over the workspace and comparing the six known measured distances between the four marker to the six distance calculated by reconstructing and triangulating the coordinates marker in the image stereo pair taken from the F-cam, using the calibration data previously calculated. Three sets of measurements were tested increasing the angle (Baseline) between the relative positions of the F-cam taking the stereo pair. In each measurement set, 40 different end-effector pose were collected. The statistical error between the known distances and reconstructed distances are shown in Table 5. The larger errors observed in the first and second set is

consistent with the fact that a larger baseline allows increasing accuracy in triangulating points

**Table 5: F-cam accuracy result**

Parameters	Error Baseline		
	Angle 20°	Angle 30°	Angle 40°
Standard Deviation [mm]	3.6	3.3	3.1
Range [mm]	7.7	6.9	6.7
Minimum [mm]	3.3	3	2.8
Maximum [mm]	11	9.9	9.5
N° Pose [mm]	40	40	40

## 6.5 Targeting

For the targeting procedure the target consisted of radiolucent spheres 2, 4 and 10 mm in diameter, placed on a screw locked in various positions of a Plexiglas board. To perform the needle alignment and insertion the required translations and rotations were computed for each position. The needle holder, with the needle inserted up to the tip of the guide, was introduced into its position on the robot end-effector. With the system adjusted and locked to the specified positions, the needle was advanced through the needle guide to a pre-ticked position on the needle, specifying final needle depth.

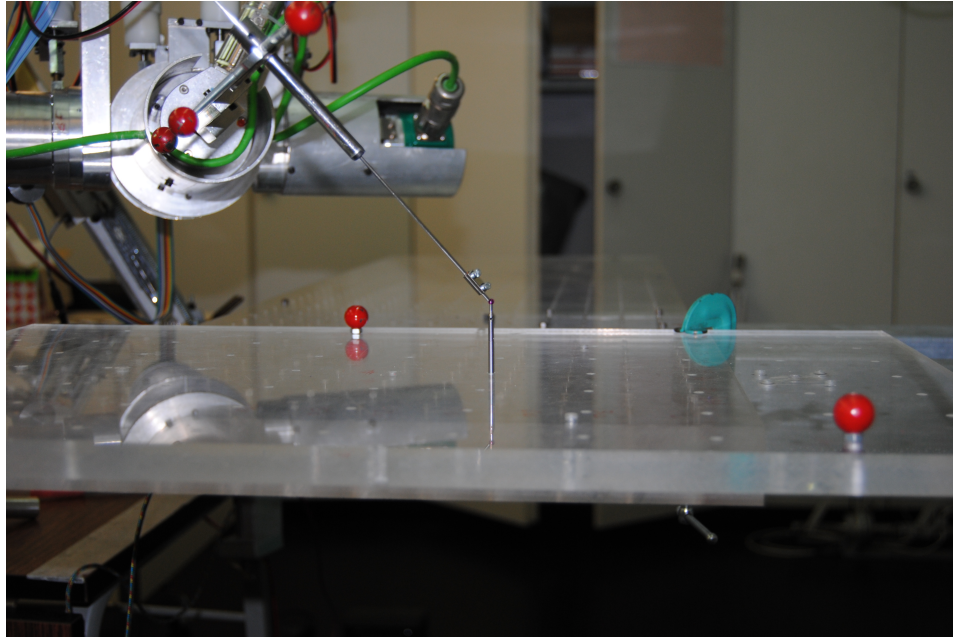


**Figure 50: Needle targeting procedure**

To evaluate the needle targeting accuracy the testing consisted of “go-no-go” tests, providing an indication to whether needle insertion was successful or not. The time to perform the procedure was about 3 min.

**Table 6: F-cam based targeting accuracy result**

Sphere diameter	Success	Failure	Success rate
10 mm	12	0	100%

## **6.6 Setup II: Registration and Targeting**

The second setup was built to test the accuracy of the system composes the Navi-Robot and the CT scan. To do so, the same Plexiglas board was provided by three spherical markers, resembling the body of the patient, and a CT scan of the object was performed.



**Figure 51: CT scan of the rigid object simulating the patient**

Both strategies described in sections 5.2, 5.3 were tested and final accuracy of the system was evaluated using the targeting procedure above mentioned. The registration procedure used for the first registration strategy is shown in the picture below: the spherical marker places on the board are holed allowing inserting a probe carried by the end-effector to a pre-defined depth. Knowing the insertion depth the center of mass of the spherical marker can be calculated in the robot coordinate system (RCS). The registration procedure is performed in sequence for each marker in order to define the position and orientation of a coordinate system associated to the body of patient.

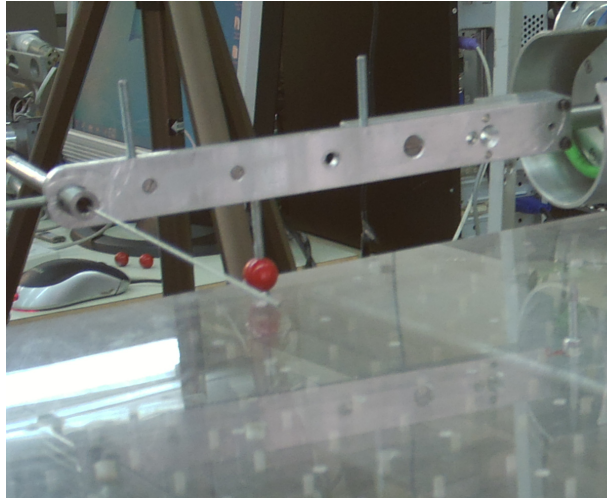


**Figure 52: Registration strategy**

Even in this case, to evaluate the needle targeting accuracy the testing consisted of “go-no-go” tests. The targeting procedure was performed 24 times for both registration approaches. The time to perform the procedure was about 3 min. using the first registration strategy and 2.5 min. for the second one excluding the time necessary to import the CT images.

**Table 7: CT based targeting accuracy result**

<b>Strategy I</b>			
Sphere diameter [mm]	Success	Failure	Success rate
2	12	0	100%
4	12	0	100%
<b>Strategy II</b>			
2	2	10	17%
4	12	0	100%



The results show a better accuracy with respect the procedure performed by using the camera simulating the fluoroscope as we can expect due the inaccuracies originated by the camera and by the calibration process.

Comparing the two strategies approach, we can notice a better accuracy for the first registration approach in the simulated environment where the rigid object used allowed rigidly linking the markers to the board and localizing them inserting a screw embedded on the end-effector. However, achieving the same result in the real surgery room environment could be more difficult. In fact the contact between the screw and the marker placed on the body of the patient could cause a displacement of the marker and thus errors in the target recovery position. A possible solution could be that to use directly the needle to localize the marker, reducing both the contact's area and the force necessary to localize the marker. As an alternative an optical localizer could be use, but this solution increase the cost of the system.

## **6.7 Error Propagation**

A number of error sources exist in the designed system. These error sources include errors originating from the calibration, point selection and repeatability of the robotic system. Despite the fact that the effect of each individual error source is impossible to describe quantitatively, a description of the possible error sources could be useful for a future work.

The errors incurred due to calibration influence the accuracy of marker targeting. In the project, error minimization techniques were tested with the aim of reducing targeting errors. The decrease in targeting accuracy outside the calibration volume can also affect the accuracy of the system. Working inside the calibration volume is crucial in avoiding large targeting errors. This implies that the height of the target volume must be identified in the pre-surgery planning stage and taken into account during the calibration and targeting stage of the procedure. The mechanical of the robotic system with a standard deviation of 0.4 mm was acceptable for the first prototype, however different

mechanical solutions could be useful to achieve better robot accuracies and repeatability in order to restrict deflection of the axes of the joints, and other geometric errors.

## **7. Conclusions and Recommendations**

### **7.1 Challenges, Future Improvements and Recommendations**

Implementation of the designed system poses some challenges. One is implementing the stereovision theory using a single camera simulation the fluoroscope. The goal was achieved using a homemade optical localizer and the relative software to localize the position of the C-arm fluoroscopy system. A limited accuracy of localizer and errors in the calibration procedure or a limited calibration volume makes are issues that could be investigated and improved.

Better optical localizer accuracy is beneficial even for using the Navi-Robot with the CT scanner. The identification of corresponding entry and target points in the image stereo pair leaves room for improvement, as the surgeon is still required to rely on his/her experience to choose the same points in two different images. Further research into methods of automatic point identification in stereo pairs would significantly increase accuracy and system confidence. Further researches should be done to design a calibration object for the real surgery room environment. A possible solution could be manufactured, for instance placing a number of metallic spherical markers on a rigid grid arranging the markers using different depth levels. With these improvements, calibration and targeting accuracy will improve, as a larger image area is calibrated. A number of improvements to the current robotic positioning system

are possible. One would be the replacement of the manual insertion by an automated alternative such as the use another servo-or stepper motors which allows the needle to translate and rotate. This would increase procedure speed reducing the risk of needle deflection during the insertion, but would increase system cost. Moreover, still leaving the chance to use passive and active mode, new mechanical solutions can be studied in order to reduce geometric errors and tolerances as well as increase step motors and encoder resolution.

An improved needle depth monitoring and insertion technique is recommended in future prototypes. The automatic technique used in the PAKY system, which makes use of two rotational discs that clamp the needle by means of friction, is a concept that can be adapted for this application [23]. Recommended changes to the current user interface include improved visual aid to the operator by means of stepwise diagrammatical illustrations and fewer GUI interactions.

Since the first version of the software was developed in Matlab, a further study aimed to convert the software into different programming languages could be helpful for a larger sharing of the software.

## **7.2 Conclusion**

The goal of this thesis was the development of an image guided robotic system for needle-positioning procedures. Such a system would aid the surgeon in inserting a needle into a tissue reducing: surgery time, surgery cost and patient-surgeon radiation exposure. Current biopsy techniques implemented in general practice rely only on surgeon experience for needle guidance and often result in sub-optimum placement of the needle inside the tissue, increased hemorrhage due to multiple unsuccessful needle punctures and in some cases, termination of the surgery due to reduced visibility and risk to the patient.

In this project, it was set out to perform needle biopsy using the Navi-Robot both under a simulated C-arm fluoroscopy and under CT.

To achieve the first goal, a stereovision setup was built using a single camera

simulating the C-arm fluoroscopy system, an optical localizer and the relative software including the graphical user interface. A new calibration technique was designed to implement the stereovision theory using a C-arm fluoroscopy system. As only a stereo image pair was required for the targeting procedure, just a fraction of the radiation dose emitted during a normal biopsy was discharged during a targeting procedure. The robotic needle-positioning system was adjusted according to the calculated values and the needle inserted to the specified depth. Simulating the C-arm fluoroscopy system with a digital camera, needle placement accuracies of 10 mm was achieved within the calibrated volume.

To achieve the second goal, or rather, to guide a biopsy procedure using the Navi-Robot under CT, a second algorithm was implemented using two registration strategies. The first one was performed using the Navi-Robot as measuring system and its end-effector as a touch probe to localize the marker placed on the simulated patient and a needle placement accuracies of 2 mm was achieved for the targeting procedure. Using CT images and the optical localizer for the registration procedure accuracies of 4 mm was obtained in the simulated environment.

The average access-procedure time of 3 minutes compares favorably to access times of current manual techniques that can range between 10 and 40 minutes. Recommendations concerning the use of the GUI implemented and simplification of certain elements of the procedure will be included in future prototypes.

## BIBLIOGRAPHY

- [1] Gordon Singer, "Occupational radiation exposure to the surgeon," *Journal of the American Academy of Orthopaedic Surgeons*, vol. 13, no. 1, pp. 69-76, Jan-Feb 2005.
- [2] Clinic Staff Mayo. (2011, March) mayoclinic. [Online].  
<http://www.mayoclinic.com/health/biopsy/CA00083>
- [3] F.S, Azar, D.N. Metaxas, and M.D Schnall, "A finite element model of the breast for predicting mechanical deformations during biopsy procedures," in *Mathematical Methods in Biomedical Image Analysis Proceedings. IEEE Workshop on*, Hilton Head Island, SC, 2000, pp. 38-45.
- [4] A Zivanovic and BL Davies, "A robotic system for blood sampling," *IEEE Transf Inform technol Biomed*, vol. 4, no. 1, pp. 8-14, 2000.
- [5] PR Rizun, PB McBeth, and DF Louw, "Robot-assisted neurosurgery," *Semin Laporasc Surg*, vol. 2, no. 11, pp. 99-106, 2004.
- [6] Z Wei, G Wan, and L Gardi, "Robot-assisted 3D-TRUS guided prostate brachytherapy: system integration and validation.," *Med Phys*, vol. 3, no. 31, pp. 539-548, 2004.
- [7] Ji Hyun Youk, Eun-Kyung Kim, Min Jung Kim, Ji Young Lee, and Ki Keun Oh, "Missed Breast Cancers at US-guided Core Needle Biopsy: How to Reduce Them," *RadioGraphics*, no. 27, pp. 79-94, 2007.
- [8] S Nath, Z Chen, N Yue, S Trumpore, and R Peschel, "Dosimetric effects of needle divergence in prostate seed implant using 125I and 103Pd radioactive seeds," *Med Phys*, vol. 5, no. 27, pp. 1058-1066, 2000.
- [9] JJ Carr et al., "Stereotactic localization of breast lesions: how it works and methods to improve accuracy," *RadioGraphics*, no. 21, pp. 463-73, 2001.
- [10] Linda T Kohn, Janet M Corrigan, and Molla S Donaldson,, 2000.
- [11] K Shimoga and P Khosla, "Visual and force feedback to aid neurosurgical," in *IEEE international conference on engineering in medicine and biology.*, Baltimore,

MD, 1994, pp. 1051-1052.

- [12] Rampersaud YR, David A Simon, and Kevin T Foley, "Application-specific accuracy requirements," in *symposium of fourth computer assisted orthopaedic surgery*, 1999.
- [13] SP DiMaio and SE Salcudean, "Needle insertion modeling and simulation," *IEEE Trans Robot Automat*, vol. 5, no. 19, pp. 864-875, 2003.
- [14] P L Roberson, Vrinda Narayana, Daniel L McShan, and Raymond J Winfield, "Source placement error for permanent implant of the prostate," *Medical Physics*, vol. 24, no. 2, pp. 251-257, 1997.
- [15] H Katoka, T Washio, M Audette, and K Mizuhara, "A model for relations between needle deflection, force, and thickness on needle insertion," in *medical image computing and computer-assisted intervention (MICCAI)*, London, 2001, pp. 966-74.
- [16] R Taschereau, J Pouliot, J Roy, and D Tremblay, "Seed misplacement and stabilizing needles," *Radiother Oncol*, no. 55, pp. 59-63, 2000.
- [17] D Stoianovici et al., "AcuBot: A Robot for Radiological Interventions," *IEEE Transactions on Robotics and Automation*, vol. 19, no. 5, 2003.
- [18] P Potamianos, BL Davis, and RD Hibberd, "Intra-operative registration for percutaneous surgery," in *International Symposium on Medical Robotics and Computer Assisted Surgery*, Baltimore, MD, 1995.
- [19] A Bzostek, S Schreiner, and A Barnes, "An automated system for precise percutaneous access of the renal collecting system," in *CVRMed-MRCAS*: Springer-Verlag, 1997, pp. 1205-1299.
- [20] A Rovetta, "Tests on reliability of a prostate biopsy telerobotic system," *Studies in Health Technology and Informatics* , vol. 62, pp. 302-307, 1999.
- [21] D Stoianovici et al., "An efficient needle injection technique and radiological guidance method for percutaneous procedures," in *CVRMed-MRCAS'97*. Springer-Verlag, 1997, vol. 1205, pp. 295-298.
- [22] Radeka, "Percutaneous Nephrostomies - Planning for an optimal access, Complications, Follow-up and Outcome," Uppsala, 2005.
- [23] J A Cadeddu, D Stoianovici, R N Chen, R G Moore, and L R Kavoussi, "Stereotactic

- Mechanical Percutaneous Renal Access," *Journal of Endourology*, vol. 12, pp. 121-125, 1998.
- [24] N C Hanumara, C J Walsh, A H Slocum, A H Gupta, and J Shepard, "Human Factors Design for Intuitive Operation of a Low-Cost, Image-Guided, Tele-Robotic Biopsy Assistant," in *29th Annual International Conference of the IEEE EMBS*, 2007, pp. 1257-1260.
- [25] R Viard et al., "Needle Positioning in Interventional MRI Procedure Real Time Optical," in *29th Annual International Conference of the IEEE EMBS*, 2007.
- [26] N Navab, M Loser, and B Geiger, "Needle placement under X-ray fluoroscopy using perspective invariants," in *Mathematical Methods in Biomedical Image Analysis IEEE Workshop on*, Hilton Head Island, SC, 2000.
- [27] M P Heilbrun, P McDonald, J C Wiker, S Koehler, and W Peters, "Apparatus and Method for Photogrammetric Surgical Localization," 6,165,181 US, 2000.
- [28] J Regn, "Device for Making a Guide Path for an Instrument on a Patient," 6,041,249 US, 2000.
- [29] Mark P Helibrun, S Koehler, P McDonald, W Peters, and C J Wiker, "Apparatus and method for photogrammetric surgical localization," US 5603318 A, 1993.
- [30] J Hong, T Dohi, M Hashizume, K Konishi, and N Hata, "An ultrasound-driven needle-insertion robot for percutaneous cholecystostomy," *Phys Med Biol*, vol. 3, no. 49, pp. 441-455, 2004.
- [31] M Perrelli et al., "Navi-Robot, a Multipurpose Robot for Medical Applications," *Scientific Journal of IFToMM "Problems of Mechanics"*, vol. 4, no. 41, 2010.
- [32] R I Hartley and A Zisserman, *Multilpe View Geometry in Computer Vision.*, 2nd ed.: Cambridge University Press, 2004.
- [33] M Moakher, "Means and averaging in the group of rotations," *SIAM Journal on Matrix Analysis and Applications*, vol. 24, no. 1, pp. 1-16, 2002.
- [34] I Sharf, A Wolf, and M B Rubin, "Arithmetic and geometric solutions for average rigid-body rotation," *Mechanism and Machine Theory*, no. 45, pp. 1239-1251, 2010.
- [35] M Vo, Z Wang, L Luu, and J MA, "Advanced geometric camera calibration for

machine vision," *Optical Engineering*, vol. 50, no. 11, 2011.